Nanocrystal Solar Cells

by

Ilan Gur

B.S. (University of California, Berkeley) 2002
M.S. (University of California, Berkeley) 2003

A dissertation submitted in partial satisfaction of the
requirements for the degree of

Doctor of Philosophy

in

Engineering-Materials Science and Engineering

in the

GRADUATE DIVISION
of the
UNIVERSITY OF CALIFORNIA, BERKELEY

Committee in Charge

Professor A. Paul Alivisatos, Chair

Professor Eicke R. Weber

Professor Peidong Yang

Fall 2006

Nanocrystal Solar Cells

by

Ilan Gur

Abstract

Nanocrystal Solar Cells

by

Ilan Gur

Doctor of Philosophy in Engineering-Materials Science and Engineering

University of California, Berkeley

Professor A. Paul Alivisatos, Chair

This dissertation presents the results of a research agenda aimed at improving integration and stability in nanocrystal-based solar cells through advances in active materials and device architectures. The introduction of 3-dimensional nanocrystals illustrates the potential for improving transport and percolation in hybrid solar cells and enables novel fabrication methods for optimizing integration in these systems. Fabricating cells by sequential deposition allows for solution-based assembly of hybrid composites with controlled and well-characterized dispersion and electrode contact. Hyperbranched nanocrystals emerge as a nearly ideal building block for hybrid cells, allowing the controlled morphologies targeted by templated approaches to be achieved in an easily fabricated solution-cast device. In addition to offering practical benefits to device processing, these approaches offer fundamental insight into the operation of hybrid solar cells, shedding light on key phenomena such as the roles of electrode-contact and percolation behavior in these cells. Finally, all-inorganic nanocrystal solar cells are

presented as a wholly new cell concept, illustrating that donor-acceptor charge transfer and directed carrier diffusion can be utilized in a system with no organic components, and that nanocrystals may act as building blocks for efficient, stable, and low-cost thin-film solar cells.

_____

Professor A. Paul Alivisatos
Dissertation Committee Chair

Table of contents

Acknowledgments

"We are like dwarfs on the shoulders of giants, so that we can see more than they, and things at a greater distance, not by virtue of any sharpness on sight on our part, or any physical distinction, but because we are carried high and raised up by their giant size."

- Bernard of Chartres

If I have accomplished anything in this life, it is because I have done so perched firmly on the shoulders of giants. I would like to take this opportunity to thank some of those colossal figures, without whom I could not have even envisioned this achievement, let alone found a path to realize it.

Paul – your example has been that of the noblest dedication to a life's work driven by heart and mind. Thank you for all that you've taught me, and for your constant support throughout this experience. Thanks also to the entire Alivisatos group and its collaborators: in particular, Neil Fromer, Michael Geier, Antonis Kanaras, Chih-Ping Chen, and Rupert Huber for their direct contributions to my research, Kevin Sivula, Mathew Law, Lori Greene, and Dmitri Talapin for their research support, Rita Tidwell and James Wang worrying about a lot of things so that I didn't have to, and Delia Milliron and Andreas Meisel for their early mentorship. Finally, thanks to all the faculty, students, staff, and administration at Berkeley for creating an environment in which anything is possible.

My parents and older brother, Saar, were of course the first "giants" in my life. Thank you for teaching, motivating, and supporting me to succeed…and for smiling with

me through it all. To my beloved Sarah – thanks for carrying my heart in yours, for treading softly on my dreams, and for being so close that your eyes close as I fall asleep….

Many more of you must go unmentioned, as it would be impossible for me to thank you all by name – you without whose love, support, inspiration, vision, motivation, energy, laughter, spirit, knowledge…without whose mere existence I would not be who I am today, nor accomplished what I have. Thank you all.

Chapter 1

Introduction

The introduction of solar cells based on organic electronic materials has incited a remarkable movement in the field of photovoltaic (PV) technologies (*1*). Organic semiconductors offer the potential to dramatically transform the economic landscape of the solar cell industry: an industry which since its inception has depended on high subsidies, or has otherwise been restricted to niche applications, due to the prohibitively high materials and processing costs of conventional technologies.

Organic solar cells demonstrate several key advantages over their conventional counterparts. Organic materials are generally lightweight and can be cheaply synthesized in large quantities. In addition, many organic systems can be processed from solution, offering the prospect of scalable, roll-to-roll device fabrication. Finally, organic PV systems are relatively insensitive to substitutional impurities, and utilize ultra-thin (~200 nm) device structures, thus dramatically reducing materials requirements relative to conventional silicon and thin-film technologies.

While the advantages of organics point toward potential economic benefits, the limitations of organic systems primarily influence device performance rather than cost. Most organic semiconductors are characterized by high energy and narrow-band absorption; as a result, only a fraction of the solar spectrum may be utilized for PV

conversion. Further reduction in conversion efficiencies arise from losses due to the exceptionally low carrier mobilities characteristic of organic semiconductors. Finally, with a strong sensitivity to photooxidation, organic solar cells are subject to severe environmental degradation. Unfortunately, despite the potential for significant cost reduction vis-à-vis conventional solar cells, these limitations have prevented organic PVs from emerging as a commercially viable technology.

Colloidal inorganic nanocrystals share all of the primary advantages of organic materials - scalable and controlled synthesis, an ability to be processed in solution, and a decreased sensitivity to substitutional doping. Meanwhile, colloidal nanocrystals retain the broadband absorption, superior transport properties, and robustness of traditional photovoltaic semiconductors (*2-4*). These materials open the door for new opportunities to create low-cost solar cells with performance and stability to enable wide-scale clean power generation.

Utilizing inorganic nanocrystals for electron transport has already been found to enhance performance in semiconducting polymer solar cells (*5, 6*). These hybrid systems perform competitively with purely organic cells; however, as with most bulk-heterojunction devices, nanocrystal-polymer cells suffer from poor morphological control and recombination losses due to the need for carriers to be transported through a disordered percolation network of donors and acceptors (*7, 8*). Recent synthetic advances have demonstrated new levels of control and manipulation over the structure and properties of colloidal nanocrystals (*9-12*). The first part of this dissertation presents research aimed at utilizing novel colloidal nanocrystals to enhance the performance of hybrid PV cells. Prescribing the structure of nanocrystals through simple synthetic

techniques allows for improved processing schemes and architectures for low-cost hybrid cells.

Despite advances in processing and morphology, hybrid solar cells will by definition always depend on an active organic component, and, consequently, hybrid systems will ultimately face the limitations to transport and stability imparted by an organic phase. A new class of solar cell based exclusively on colloidal nanocrystals has been anticipated theoretically in recent years (*13*). The second part of this dissertation describes the design and demonstration of such a device, and presents a number of studies to elucidate a mechanism for its operation in the context of organic donor-acceptor and conventional p-n junction solar cells. This entirely inorganic donor-acceptor solar cell offers a system that utilizes the versatile and low cost processing characteristic of organic systems, but is no longer subject to the limitations of organics. From a conceptual standpoint, this demonstration elucidates a new class of solar cells, which are wholly inorganic, but operate by means of the diffusion assisted donor-acceptor heterojunction mechanism characteristic of organic systems. This discovery offers valuable insight to help narrow the conceptual gap between organic photovoltaics and conventional systems, sheds light on new parallels between systems of colloidal nanocrystals and organic molecules, and may pave the road toward nanocrystal based solar cells that are low-cost, efficient, and stable (*14*).

References and notes

1. S. E. Shaheen, D. S. Ginley, G. E. Jabbour, *Mrs Bulletin* **30**, 10 (JAN, 2005).
2. A. P. Alivisatos, *Journal of Physical Chemistry* **100**, 13226 (AUG 1, 1996).
3. C. B. Murray, C. R. Kagan, M. G. Bawendi, *Annual Review of Materials Science* **30**, 545 (2000).
4. M. Shim, C. J. Wang, D. J. Norris, P. Guyot-Sionnest, *Mrs Bulletin* **26**, 1005 (DEC, 2001).
5. W. U. Huynh, J. J. Dittmer, A. P. Alivisatos, *Science* **295**, 2425 (MAR 29, 2002).
6. B. Q. Sun, E. Marx, N. C. Greenham, *Nano Letters* **3**, 961 (Jul, 2003).
7. W. U. Huynh, J. J. Dittmer, W. C. Libby, G. L. Whiting, A. P. Alivisatos, *Advanced Functional Materials* **13**, 73 (Jan, 2003).
8. J. S. Liu, T. Tanaka, K. Sivula, A. P. Alivisatos, J. M. J. Frechet, *Journal of the American Chemical Society* **126**, 6550 (Jun 2, 2004).
9. L. Manna, D. J. Milliron, A. Meisel, E. C. Scher, A. P. Alivisatos, *Nature Materials* **2**, 382 (JUN, 2003).
10. X. G. Peng *et al*., *Nature* **404**, 59 (MAR 2, 2000).
11. L. Manna, E. C. Scher, A. P. Alivisatos, *Journal of the American Chemical Society* **122**, 12700 (DEC 27, 2000).
12. D. J. Milliron *et al*., *Nature* **430**, 190 (JUL 8, 2004).
13. A. J. Nozik, *Physica E-Low-Dimensional Systems & Nanostructures* **14**, 115 (APR, 2002).
14. I. Gur, N. A. Fromer, M. L. Geier, A. P. Alivisatos, *Science* **310**, 462 (October 21, 2005, 2005).

Chapter 2

Hybrid nanocrystal-polymer solar cells

2.1 Introduction

Solar cells incorporating both organic semiconductors and inorganic semiconductor nanocrystals aim to integrate the benefits of both classes of materials. Inorganic semiconductors are ideal for fabricating highly efficient solar cells as they absorb a broad range of light and transport charge effectively. However, bulk inorganics require expensive processing, historically limiting the cost effectiveness of conventional inorganic solar cells. This has motivated extensive research on organic photovoltaic cells since small molecule and especially polymer semiconductors can be inexpensively processed into flexible, thin film photovoltaics. Semiconductor nanocrystals combine many advantageous characteristics of bulk inorganic materials with the solution processibility and low temperature chemical synthesis of polymers. Additionally, the optical gap of inorganic nanocrystals can be tuned by material selection and quantum confinement, and synthetic advances allow control over nanocrystal size and shape to optimize photovoltaic performance. Hybrid solar cells blending organic semiconductors and inorganic semiconductor nanocrystals offer the potential to deliver efficient energy conversion with low cost fabrication.

The development of hybrid solar cells followed a period of rapid growth in the field of thin film organic photovoltaics. The introduction of composite or blend architectures in 1995 (*1-3*) marked a significant innovation over the original bilayer organic heterojunction cell demonstrated almost 10 years prior (*4*). Photovoltaic cells with an active layer consisting of a blend of materials are based on a bulk donor–acceptor heterojunction. In contrast to a planar heterojunction, the large area interface formed between the blended materials delocalizes the charge–separating region throughout the film. The blend design led to enhanced performance in cells composed of two different polymers, and verification of the concept has recently been extended to small molecule systems (*1, 2, 5*). Still, the most significant advances in organic–based cells have come from the utilization of fullerene derivatives as a cell component, first reported by Yu and coworkers for the case of PCBM, a derivative of C60 (*3*). While C60 does not act as an active absorber, it is highly effective in separating and transporting charge such that power conversion efficiencies nearing 5% have been realized in bulk heterojunction polymer cells incorporating C60 derivatives (*6*). Nanocrystal-based solar cells, in which semiconductor nanocrystals make up at least one of the blend components, constituted a natural progression. Not only does the nanocrystal component serve as an active absorbing material in such devices, the absorption properties can be tuned by means of quantum confinement, allowing for further optimization.

In a general bulk heterojunction solar cell, the active blend layer is sandwiched between a transparent (front) and a reflecting (back) electrode (Figure 2.1). The blended materials are commonly processed from solution, creating inexpensive options for scaled up fabrication, including roll–to–roll processing made possible by the use of flexible substrates. Light is incident through the front electrode and absorbed in one or more of the active blend components. The resulting excitons can thermally dissociate to spatially separated electrons and holes; in polymers, however, they more often remain bound due to a significant exciton binding energy. In this case, they diffuse randomly until geminate recombination occurs or until they reach an interface. The semiconductor–electrode interfaces can serve as a site for charge separation, but since the exciton diffusion length in polymers is typically only about 5-10 nm, very few of the excitons created are within reach of these interfaces. Rather, the distributed interface between the blend components is designed by proper alignment of energy levels to efficiently separate charges from excitons created throughout the active blend layer, leaving electrons in one blend component and holes in the other.

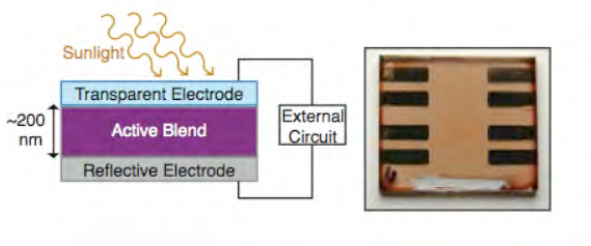

Figure 2.1 (a) Schematic layout of a bulk heterojunction solar cell. The active layer is cast from a cosolution of blend components including semiconductor nanocrystals. The active layer should be sufficiently thick to absorb most of the incident light. (b) Photograph of a substrate containing 8 active devices prepared in our lab.

Following charge transfer, the separated carriers must be transported through the blend to the electrodes. The holes and electrons will be transported through different components of the blend, so a continuous path through each material is necessary for

effective transport. Since the cell cannot accumulate charge indefinitely and maintain an electric field, the least mobile carrier often limits performance. In addition, the requirement for interpenetrating, percolating networks creates a strong dependence of efficiency and reproducibility on blend morphology. The final step in the energy conversion process involves the collection of charges by the electrodes, which carry them to the external circuit. Limited research exists on the efficiency of this process in blend photovoltaics.

Materials selection for blend cells must reflect the requirements of each step in the energy conversion process. The π–π^* absorption in semiconducting polymers can be rather strong, but occurs over a discreet energy range, covering only part of the solar spectrum. As such, blends should ideally incorporate materials with complementary absorption, preferably extending into the often difficult to achieve near infrared (NIR) range. As an additional design criterion, the driving force for charge transfer must exceed the sum of the exciton binding energy and the charge separation energy. Finally, effective transport of both carriers depends on the their inherent mobility and on sufficient morphology control to achieve percolation. This collection of simultaneous constraints represents a daunting challenge in polymer design to reach the full potential of polymer blend solar cells.

Incorporating inorganic semiconductor nanocrystals as a component in the blend can address many of these challenges. Light absorption in inorganic semiconductors begins at the band edge and increases toward higher energy without falling off. In direct gap semiconductors, this absorption can be quite strong and can be enhanced in nanocrystals by quantum confinement effects. In addition, depending on material choice,

absorption can easily extend through the red and into the NIR range of the solar spectrum. Energy levels of inorganic semiconductors naturally differ from those of organic semiconductors, and are typically well aligned for charge transfer. Finally, charge transport within a nanocrystal is very effective; it is at least as efficient as band transport and may be ballistic in some cases. In polymers, achievable hole mobilities far exceed electron mobilities. This discrepancy favors the introduction of inorganic semiconductor nanocrystals to transport electrons. The remainder of this chapter will examine the design, fabrication and operation of hybrid solar cells based on inorganic nanocrystals.

2.2 Inorganic nanocrystals for solar cells

Colloidal nanocrystals are nanometer scale crystals that echo properties of the corresponding bulk material, but also have distinct size dependent properties. They are coated with a surfactant that mediates their growth and facilitates their dispersion in either common organic solvents or, alternatively, in water. Organic solvents are compatible with conjugated polymers, so surfactants with nonpolar tails are favored for preparing blend photovoltaics. Cadmium selenide (CdSe) is a prototypical material for semiconductor nanocrystals with well developed syntheses and widely studied photophysical properties (*7*). These nanocrystals are synthesized by nucleation from organometallic precursors in a hot liquid mixture of surfactants (250–350 °C) and remain coated with a monolayer of surfactant after synthesis. This monolayer allows for stable dispersion in organic solvents.

Using this basic synthetic strategy, controlled sizes and shapes of nanocrystals have been prepared with narrow distributions, and systematic variations in photophysical properties have been demonstrated (Figure 2.2). Different sizes of CdSe spheres from approximately 2 to 12 nm have been prepared by varying precursor concentrations and the time that the nanocrystals are allowed to grow before cooling the reaction mixture (*8*). Rod shaped nanocrystals result from extended growth along the unique c-axis of the hexagonal wurtzite structure, which is achieved by varying the surfactant mixture (particularly by including alkylphos- phonic acids) or the concentration of the precursors (*9*). Branched CdSe nanocrystals incorporate regions of the cubic zincblende structure at their branch points (*10*). These nanocrystals occupy three-dimensional space, making them particularly promising for transporting charge in blend photovoltaics.

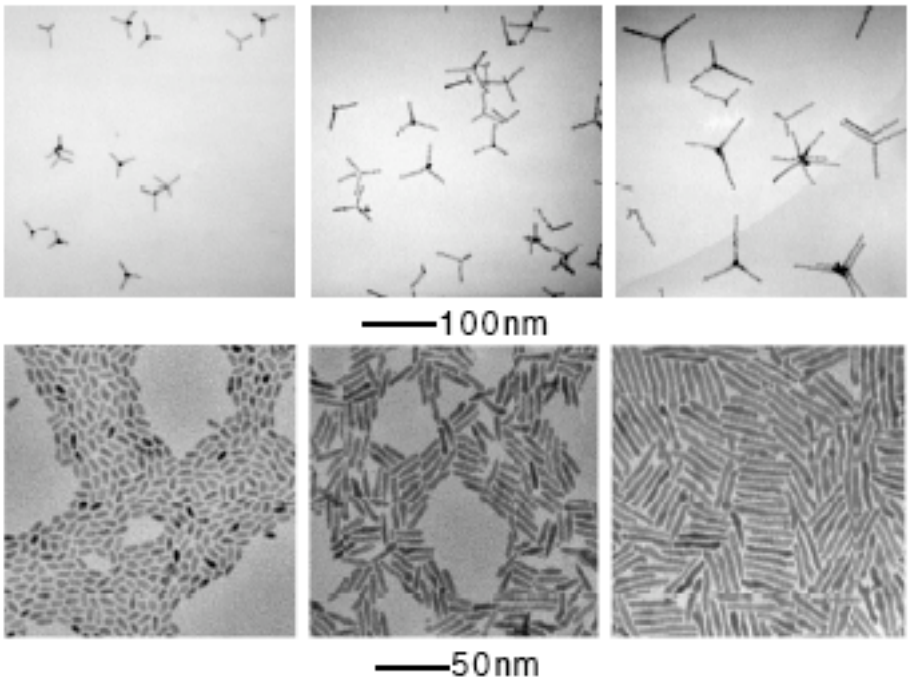

Figure 2.2: A gallery of semiconductor nanocrystals viewed by transmission electron microscopy. (a) CdSe rods of different lengths, with diameter held relatively constant. (b) CdTe tetrapods with different arm lengths, again with diameter held constant.

The optical band gap of semiconducting nanocrystals is size dependent due to quantum confinement. When the size of a semiconductor sphere approaches the Bohr radius of the bulk exciton, quantum confinement effects become substantial (*11*). The energy of the exciton is increased and the optical band gap shifts to the blue (Figure 2.3). Excitons in nanorods and in the arms of branched nanocrystals are confined mostly along the diameter since the length often exceeds the exciton radius by several times (*12*). In all cases, quantum confinement can enhance the oscillator strength for absorption (*13*) by

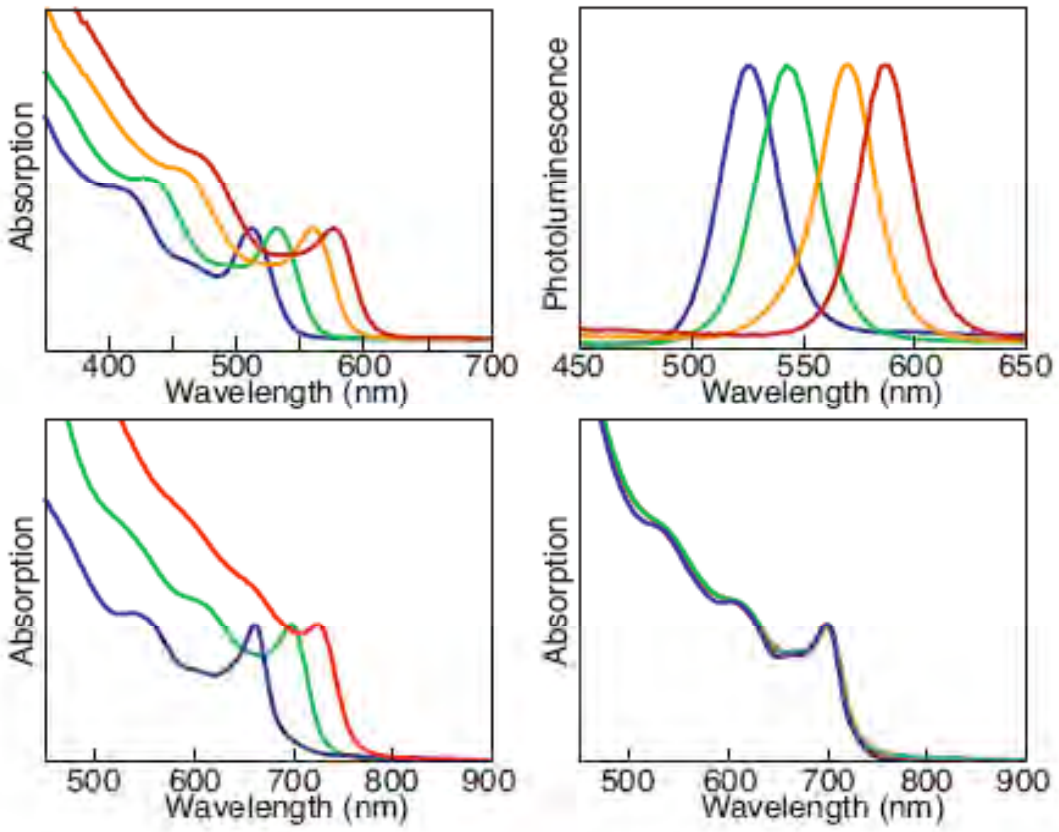

Figure 2.3: UV-visible absorption spectra (a) and photoluminescence spectra (b) for different sizes of CdSe nanospheres. The band gap shifts due to quantum confinement, and peaks correspond to exciton energy levels. Similarly the UV-visible absorption spectra for CdTe tetrapods (c) with arms of similar length, but different diameters and (d) with arms of similar diameter, but different lengths.

concentrating the exciton into a smaller region. Ultimately, broad tunability of the band gap within a single material system will enable optimal solar cell efficiencies in multiple band gap cells (*14*).

2.3 Incorporating nanocrystals into active hybrid blends

To take advantage of properties of inorganic nanocrystals, they must be processed into a blend solution and cast into a film as the active layer of a solar cell. While the nanocrystals as synthesized are soluble in organic solvents and readily miscible with conjugated polymers, their electronic interaction with each other and the surrounding polymer is inhibited by their insulating surfactant coating (*15*). Surfactant exchange through mass action by refluxing or repeated washing in pyridine has been shown to remove much of the original surfactant on CdSe, CdS, and CdTe nanocrystals. Pyridine acts as a labile ligand on the nanocrystal surface that effectively maintains their dispersion, but is easily displaced in solution or removed from a dried film under vacuum. Comparing blends of native versus pyridine-stripped nanocrystals with the photoluminescent poly(phenylenevinylene) derivative MEH-PPV15 illustrates the impact of the native surfactant on electronic accessibility. Charge transfer is indicated by quenching of polymer photoluminescence and by the appearance of photoinduced absorption bands assignable to the radical cation (*16*). While complications arise from differences in blend morphology, a near total suppression of charge transfer is evident in blends with surfactant-coated nanocrystals.

Removing the surfactant to permit electronic interaction limits nanocrystal processibility, which then relies on a favorable interaction between the semiconductor surface and the solvent. Early attempts at blending 5 nm CdSe nanospheres with MEH-PPV15 and, later, short (8 by 13 nm) CdSe nanorods (*17*) with regioregular poly(3-hexylthiophene) (P3HT) succeeded in using chloroform as a cosolvent for the polymer and nanocrystals in order to cast blend films. The small amount of pyridine remaining from the surfactant exchange reaction was sufficient to stabilize the nanocrystals in the dispersion and prevent large-scale phase separation in the blend film. The limited phase separation that did occur improved the percolation of the nanocrystals and thereby the transport of electrons through the blend. This is similar to the nanometer scale separation that was observed in optimized polymer blend cells (*18*).

For larger nanocrystals, including nanorods and branched particles, the amount of aggregation can easily exceed the desirable nanoscale separation. Such large-scale aggregation decreases light collection through scattering, reduces interfacial area needed for charge separation, and increases film roughness, creating inhomogeneities in the electric field. Aggregation can be reduced by mixing pyridine and chloroform as solvents for the cosolution of polymer and nanocrystals (*19*). Surface roughness, determined by AFM, can be a useful indicator of blend morphology since it is increased by aggregation. The minimum roughness is found for CdSe/P3HT blends cast from a solvent mixture with approximately 1 to 10% pyridine in chloroform, depending on nanocrystal shape and the extent of surfactant exchange. This represents enough pyridine to act as a surfactant for the nanocrystals, but not so much that the mixture becomes too poor a solvent for the polymer. This minimum roughness, furthermore, correlates with the

minimum photoluminescence efficiency of the P3HT (indicating maximum charge transfer) and the maximum external quantum efficiency (EQE) of the associated photovoltaic cells.

2.4 Charge transport in nanocrystal blend solar cells

Unlike polymer blend cells, the minimum amount of phase separation in CdSe nanorod–polymer blends gives rise to the greatest photovoltaic performance. This result implies that large nanorod aggregates are not necessary for effective charge transport. In polymer blends, there is an optimal degree of phase separation at which percolating transport networks are balanced against the area of the distributed hetero junction (*18*). The difference can be understood by noting that transport within a single nanorod is likely to be highly efficient. Electrical characterization of (somewhat larger) single nanowires has indicated highly effective bandlike transport (*20*). As such, electron mobility in films of nanocrystals (*21*), and in nanocrystal–polymer blends, is limited by nanocrystal–nanocrystal hopping.

Reducing the number of nanocrystal–nanocrystal hopping events that an electron must undergo to traverse a blend film improves transport efficiency. This was demonstrated for CdSe nanorod based cells by comparing different length nanorods (*22*). Photovoltaic performance was evaluated for cells containing 7 nm diameter spheres, 30 nm long rods, and 60 nm long rods. In each case the morphology was optimized and the resulting trend was a monotonic improvement in the EQE with rod length. The best cells showed a 1.7% power conversion efficiency (PCE) under AM1.5G solar conditions with

a fill factor (FF) of 0.4, and open circuit voltage (Voc) of 0.7 V. In a separate study comparing nanorods and branched nanocrystals blended with OC1 C10 -PPV, branching was found to nearly double the EQE (*22*). The three dimensional nature of the branched nanocrystals further reduces the number of charge hopping steps compared to nanorods which can tend to lie parallel to the plane of the film. A PCE of 1.8% was achieved under solar conditions, with a FF of 0.35 and Voc of 0.65.

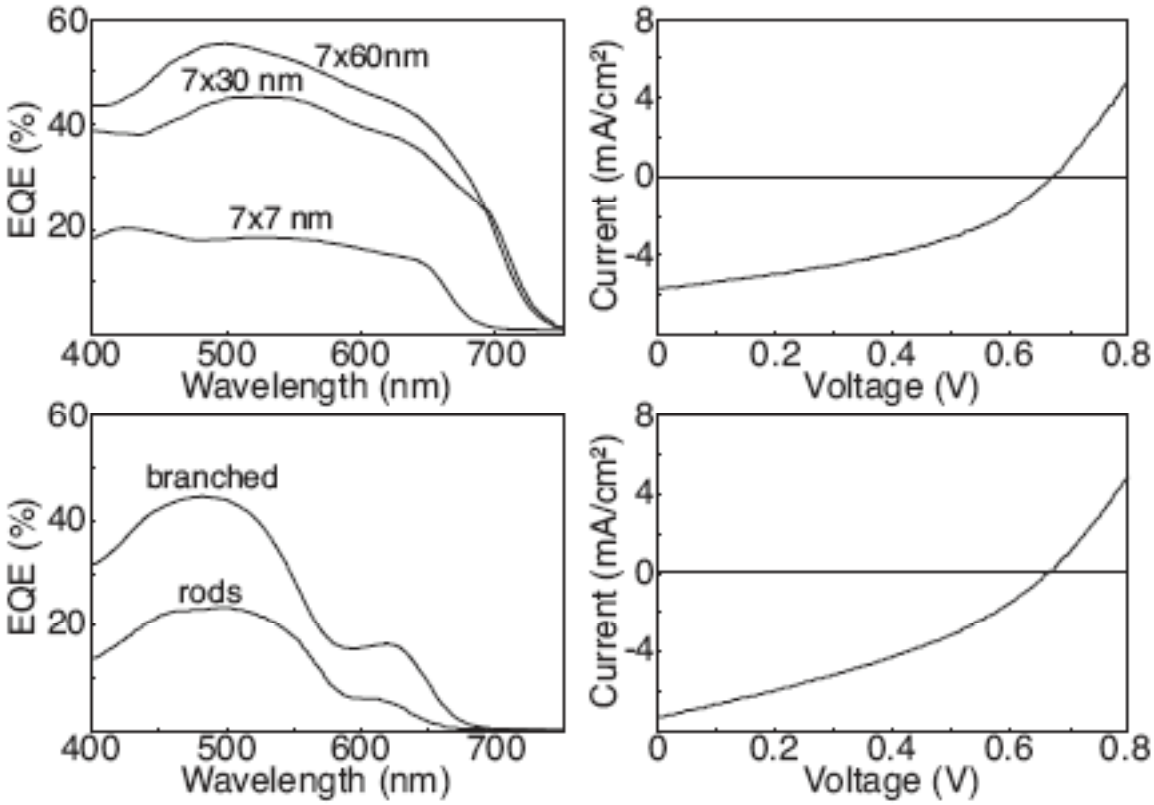

Figure 2.4: (a) Dependence of EQE on nanorod length for CdSe-P3HT hybrid solar cells. (b) Current-voltage characteristics of an optimized CdSe nanorod–P3HT solar cell under AM1.5G standard solar conditions. (c) Comparison of EQE for CdSe rods and branched nanocrystals in OC1C10-PPV. (d) Current-voltage characteristics of a branched CdSe–OC1C10-PPV solar cell under AM1.5G conditions.

2.5 The next generation of hybrid nanocrystal-polymer solar cells

The full potential of hybrid nanocrystal–polymer solar cells has yet to be realized. New advances will be driven by development of new materials, particularly nanocrystals of novel shape and composition. The recently reported branched cadmium telluride (CdTe) tetrapod nanocrystals (*23*) (Figure 2b) have potential advantages over CdSe rods and branched particles. The smaller band gap of CdTe (1.5 eV in the bulk) allows for improved absorption of the solar spectrum. Also, like branched CdSe particles, CdTe tetrapods are three dimensional, allowing for improved electron transport; their four rod-like arms project symmetrically from a central core, ensuring a transport path across the blend film regardless of their orientation. The first part of this dissertation will focus on new results describing the use of three dimensional nanocrystals in hybrid PV cells, incorporating tetrapod structures as well as newly discovered hyperbranched crystals to optimize transport and ease processing of these devices.

References and notes

1. G. Yu, A. J. Heeger, *Journal of Applied Physics* **78**, 4510 (1995/10/01/, 1995).
2. J. J. M. Halls *et al.*, *Nature* **376**, 498 (AUG 10, 1995).
3. G. Yu, J. Gao, J. C. Hummelen, F. Wudl, A. J. Heeger, *Science* **270**, 1789 (DEC 15, 1995).
4. C. W. Tang, *Applied Physics Letters* **48**, 183 (JAN 13, 1986).
5. P. Peumans, S. Uchida, S. R. Forrest, *Nature* **425**, 158 (SEP 11, 2003).
6. R. S. R. F. Padinger, N.S. Sariciftci,, *Advanced Functional Materials* **13**, 85 (2003).
7. A. P. Alivisatos, *Science* **271**, 933 (FEB 16, 1996).
8. C. B. Murray, D. J. Norris, M. G. Bawendi, *Journal of the American Chemical Society* **115**, 8706 (SEP 22, 1993).
9. X. G. Peng *et al.*, *Nature* **404**, 59 (MAR 2, 2000).
10. L. Manna, E. C. Scher, A. P. Alivisatos, *Journal of the American Chemical Society* **122**, 12700 (DEC 27, 2000).
11. M. G. Bawendi, M. L. Steigerwald, L. E. Brus, *Annual Review of Physical Chemistry* **41**, 477 (1990).
12. L. S. Li, J. T. Hu, W. D. Yang, A. P. Alivisatos, *Nano Letters* **1**, 349 (JUL, 2001).
13. W. W. Yu, L. H. Qu, W. Z. Guo, X. G. Peng, *Chemistry of Materials* **15**, 2854 (JUL 15, 2003).
14. Martin A. Green, *Progress in Photovoltaics: Research and Applications* **9**, 137 (2001).
15. N. C. Greenham, X. G. Peng, A. P. Alivisatos, *Physical Review B* **54**, 17628 (DEC 15, 1996).
16. D. S. Ginger, N. C. Greenham, *Synthetic Metals* **101**, 425 (MAY, 1999).
17. W. U. Huynh, X. G. Peng, A. P. Alivisatos, *Advanced Materials* **11**, 923 (AUG 3, 1999).
18. A. C. Arias *et al.*, *Macromolecules* **34**, 6005 (Aug 14, 2001).
19. W. U. Huynh, J. J. Dittmer, W. C. Libby, G. L. Whiting, A. P. Alivisatos, *Advanced Functional Materials* **13**, 73 (Jan, 2003).
20. Y. Cui, Z. H. Zhong, D. L. Wang, W. U. Wang, C. M. Lieber, *Nano Letters* **3**, 149 (Feb, 2003).
21. D. S. Ginger, N. C. Greenham, *Synthetic Metals* **124**, 117 (OCT 3, 2001).
22. B. Q. Sun, E. Marx, N. C. Greenham, *Nano Letters* **3**, 961 (Jul, 2003).
23. L. Manna, D. J. Milliron, A. Meisel, E. C. Scher, A. P. Alivisatos, *Nature Materials* **2**, 382 (JUN, 2003).

Chapter 3

Controlled assembly of hybrid bulk-heterojunction solar cells

3.1 Introduction

Excitonic solar cells hold great promise for enabling the production of large-scale solar power at low costs (*1*). The most efficient of these cells utilize a type II donor-acceptor heterojunction to facilitate the separation of otherwise bound excitons (*2*). Donor-acceptor cells based on simple planar architectures are limited in thickness, and in turn efficiency, by small exciton diffusion lengths. Yet when donor and acceptor materials are blended to create an interspersed or bulk heterojunction, cells can be made thick enough for strong absorption while still allowing for efficient charge separation (*3, 4*).

Nanocomposite bulk-heterojunctions constitute the most efficient class of polymer-based solar cells; however, their superior performance is contingent upon on a complex architecture that is extremely difficult to control (*5-10*). The ideal nanocomposite solar cell architecture allows the small domain sizes and large interfacial area required for optimal charge separation while still providing directed pathways for rapid carrier conduction to a set of carrier-selective electrodes. The majority of actual bulk heterojunction cells are fabricated by co-deposition of a random donor/acceptor

composite from solution, and though simple and inexpensive, this process offers little control over parameters such as blend morphology and electrode contacts, which are critical in determining the ultimate cell performance. Even characterizing the structure of co-deposited films can prove a difficult task, requiring one to rely on indirect indicators such as surface roughness or final device performance to infer the quality of the blend (*11*).

The limitations of co-deposited bulk heterojunction blends are readily evident in traditional hybrid polymer-nanocrystal solar cells, which consist of a hole-conducting polymer, poly(3-hexylthiophene) (P3HT), blended with inorganic semiconductor nanocrystals (*12, 13*). Typically, hybrid composites are co-deposited via spin-casting from a solution containing both pyridine and chloroform. An optimal mixture of these two solvents can stabilize both the organic and inorganic phases, thereby allowing for deposition of an intimate random blend film. Unfortunately, the perfect solvent mixture is hard to ascertain, and the ultimate blend morphology remains highly sensitive to solvent concentrations as well as variations in the nanocrystal synthesis and processing (*11, 14*). Blend defects such as islands and aggregation are common, and while varying the type and proportions of solvents used can help mitigate their effects and improve device performance(*15*), the random nature of the blend film inhibits alignment of the blend domains, interfering with the conduction and extraction of photoexcited carriers (Fig 3.1A). In this chapter, we present a technique to create ordered and easily characterized hybrid composites by sequential deposition of tetrapod-shaped cadmium telluride (CdTe) nanocrystals and P3HT.

3.2 Ordered composites by sequential deposition

We have previously demonstrated that tetrapod-shaped CdTe nanocrystals can be readily synthesized and prepared in solution, with a wide range of control over arm diameter and length (*16*). We now show that such nanocrystals can be used as a template for creating ordered composite structures with controlled dispersion. Figure 3.1 schematically illustrates the desired architecture (3.1B), and presents a transmission electron micrograph of the tetrapod nanocrystals utilized in this study (3.1C). The composite fabrication approach is simple. First, nancrystal tetrapods are deposited on an electrode surface. Deposition can be achieved via spin-casting or, alternatively, an amphiphilic linker molecule may be used to anchor the nanocrystals to the desired surface (*17*). At this stage, the nanocrystal density and dispersion on the surface can

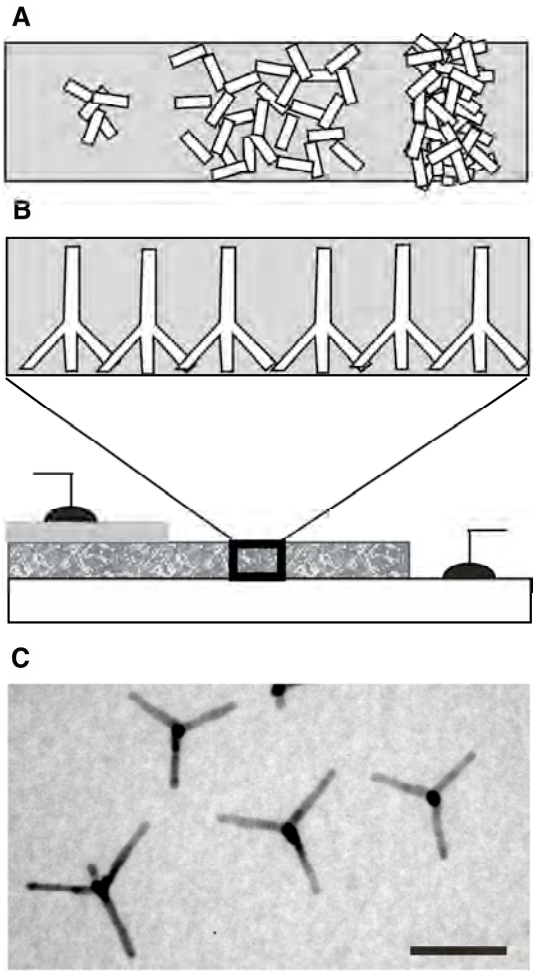

Figure 3.1: A simple schematic juxtaposes the cross-sectional morphology of traditional hybrid nanocrystal-polymer solar cells (A) with that of ordered hybrid devices based on tetrapod nanocrystals (B). Defects such as islands and aggregates detrimental to the performance of conventional hybrid cells are eliminated in ordered arrays of tetrapods, which provide directed transport to electrodes. In **C**, a transmission electron micrograph shows the tetrapod nanocrystals used in this study. Scale bar, 100nm.

be easily characterized by scanning electron microscopy. The unique tetragonal structure of the nanocrystals gives rise to a natural ordering in the deposited films; three arms of each tetrapod contact on the substrate at its base while the fourth arm points up, perpendicular to the substrate. This ordering remains evident in the composite films, created by spin-casting a polymer from its optimal solvent to cover the nanocrystal film. Tetrapod-shaped cadmium telluride nanocrystals were synthesized as previously reported using standard air-free techniques (*16*). Synthesized particles were washed 2x by dissolution in toluene and subsequent precipitation with isopropanol, then suspended in 20 mL pyridine and stirred under reflux overnight for comprehensive ligand exchange. After reflux, the nanocrystals were precipitated with hexane, washed with toluene, and redissolved in pyridine to create a dilute solution.

Fig 3.2 presents SEM micrographs illustrating the wide range of control over nanocrystal dispersions achievable by various deposition methods. Imaging the array of nanocrystals created by any one deposition approach allows for a direct measure of the crystal loading and dispersion that will appear in the ultimate blend film. In Fig 3.2A, CdTe tetrapods are anchored to a gold substrate via the linker molecule hexane dithiol. Figs 3.2B-D show similar arrays of nanocrystals, here anchored to ITO substrates by means of carboxylic acid or siloxane functionalities. After depositing one layer of nanocrystals, it is possible to anchor a second layer to the surface (Fig 3.2E). Repeating this procedure can yield even denser nanocrystals arrays. In choice of linker molecule and number of deposition steps, one can thus tailor the loading of nanocrystals that will appear in the final composite film. Finally, extremely dense nanocrystals films can be

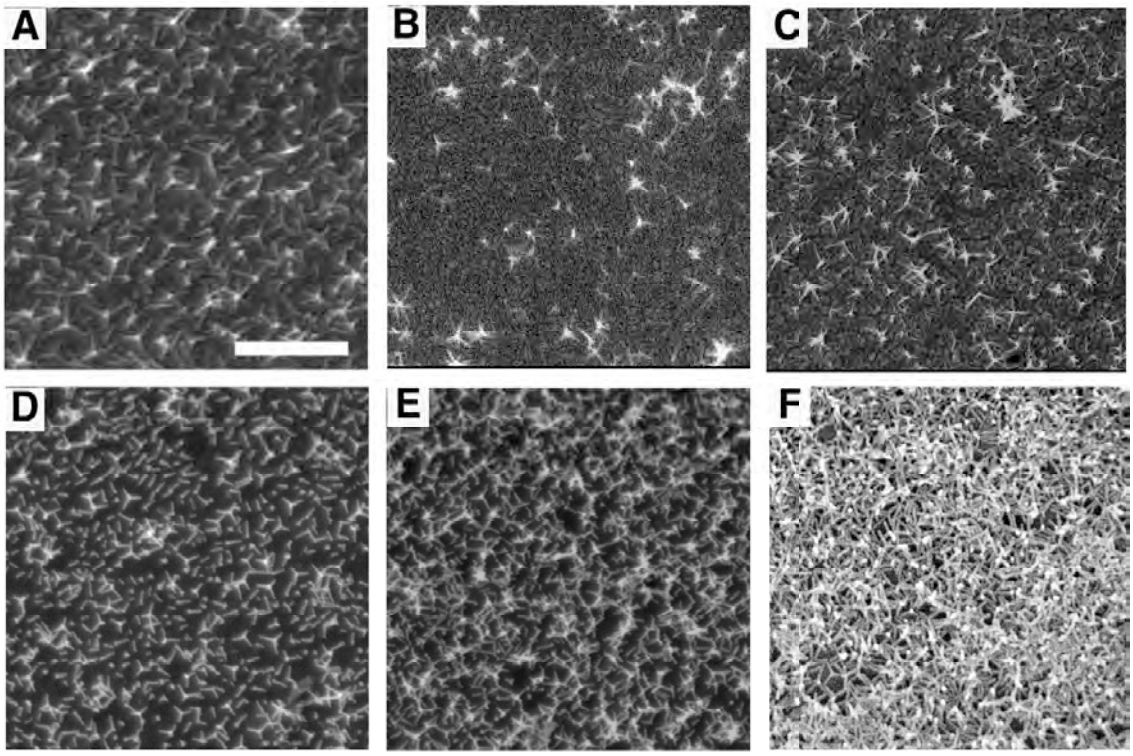

Figure 3.2: Scanning electron micrographs show arrays of CdTe tetrapods used as templates for hybrid composites. Tetrapods may be anchored to gold substrates by hexanedithiol (A) or to ITO substrates with the following linker molecules: 3-mercaptopropionic acid (B), 11-mercaptoundecanoic acid (C), mercaptopropyl trimethoxysilane (**D**). In (**E**), a second layer of tetrapods has been anchored to the film shown in (**D**). Finally, spincasting can be used to produce very dense template films on a variety of substrates (**F**). Scale bar 500 nm.

deposited via spin-casting (Fig 2F). Specific deposition procedures and conditions were as follow:

Fabrication of tetrapod monolayers on gold substrates:

10 nm chromium and 50 nm gold were thermally deposited on glass substrates. Substrates were immersed in a 5mM solution of hexanedithiol (Aldrich) in ethanol for five hours, and then rinsed for 30 seconds with pure ethanol. In inert atmosphere,

substrates coated with hexanedithiol were immersed in a dilute solution of tetrapods in pyridine for 18 hours, and then rinsed for 30 seconds with pure pyridine.

Fabrication of tetrapod of tetrapod monolayers on ITO substrates:

Carboxylic acid based linkers. Glass substrates coated with 150 nm ITO (Thin Film Devices Inc., resistivity 20 ohms/sq) were cleaned with organic solvents and exposed to oxygen plasma for five minutes. Substrates were immediately immersed in a 0.5mM solution of the linker molecule in ethanol for 18 hours, and then rinsed for 30 seconds in pure ethanol. 3-mercaptopropionic acid (Aldrich) and 11-mercaptoundecanoic acid (Aldrich) were employed independently as linker molecules. In inert atmosphere, substrates coated with linker molecules were immersed in a dilute solution of tetrapods in pyridine for 18 hours, and then rinsed for 30 seconds with pure pyridine.

Mercaptopropyl trimethoxysilane linker. Glass substrates coated with 150 nm ITO (Thin Film Devices Inc., resistivity 20 ohms/sq) were cleaned with organic solvents, immersed in a 5:1:1 H20:H2O2:NH3 solution for one hour at 70 °C, rinsed with pure H2O, and dried in oven at 120 °C for 3 hours. Substrates were immediately transferred to inert atmosphere and immersed in a 4% solution of mercaptopropyl trimethoxysilane (Aldrich) in dry toluene at 108 °C. After 24 hours, substrates were removed and rinsed with pure dry toluene. Substrates coated with mercaptopropyl trimethoxysilane were then immersed in a dilute solution of tetrapods in pyridine for 18 hours, and then rinsed for 30 seconds with pure pyridine.

Figure 3.3 shows several hybrid composites created by this approach. Since a single template of nanocrystals deposited on ITO (Fig 3.3A) was used for all composite

films, the loading and dispersion of nanocrystals remain constant across the series. However, the figure illustrates a further degree of control afforded in creating nanocrystal-polymer composites by this approach. By varying the concentration of the solution from which the polymer is spin-cast, the height to which the polymer matrix covers the original nanocrystal template array can be easily adjusted. Composites can thus be created in which much of the nanocrystals remain exposed (Fig 3.3B), or only the tips of the nanocrystals remain exposed (Fig 3.3C). Increasing the concentration of

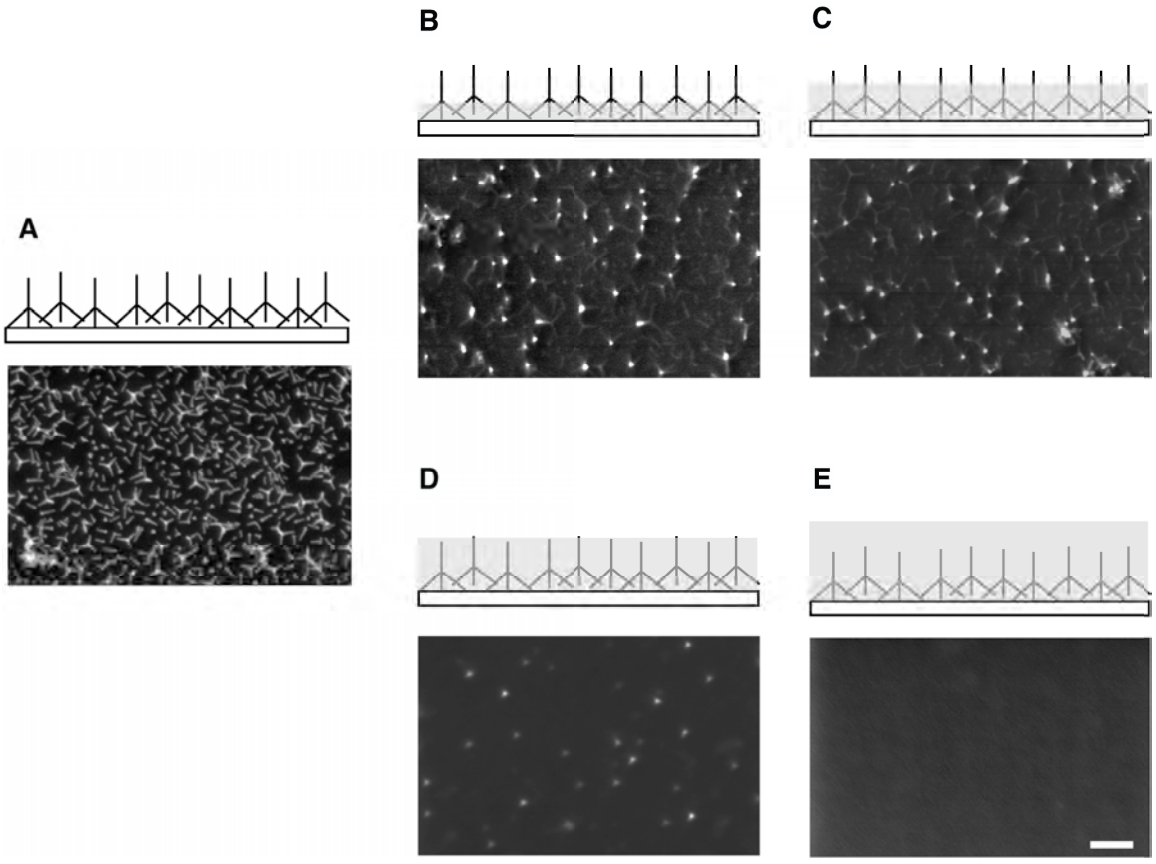

Figure 3.3: Scanning electron micrographs of an original template tetrapod array on ITO (A) and several composites produced by subsequent deposition of P3HT. P3HT was spincast from solution in chloroform with concentrations 5 mg/ml (**B**), 7.5 mg/ml (**C**), 10mg/ml (**D**), and 15 mg/ml, allowing for controlled thickness and exposure of the inorganic nanocrystals. Scale bar 200nm.

P3HT yields films in which the nanocrystals are embedded within the polymer matrix (Fig 3.3D). Finally, the most concentrated polymer solutions yield composites with nanocrystals deeply embedded (Fig 3.3E). This wide range of architectures is fabricated simply by varying the concentration of spin-cast P3HT in solution from 5 mg/ml to 15 mg/ml. Such control is of particular interest in the fabrication of electronic devices, allowing for intentional and determinate contact by the top electrode to either only one particular phase or to both phases simultaneously.

3.3 PV devices based on ordered composites by sequential deposition

Preliminary studies of photovoltaic devices based on the controlled composites shown in Fig. 3.3 show well-defined trends as a function of polymer deposition. Device characteristics for this set of cells appear in Fig 3.4. In Fig 3.4A, photoresponse spectra are shown as a function of P3HT thickness. When the tetrapods are only partially covered, we see a large photocurrent peak corresponding to the P3HT absorption, as well as a small tail resulting from the CdTe absorption. Yet upon fully covering the tetrapods, the quantum efficiency drops dramatically, as electrons are blocked from being transported to the anode. The photocurrent tail from CdTe absorption disappears entirely in these cases, and the photocurrent that does remain is likely produced at the P3HT/electrode interfaces. The current-voltage data in Fig 3.4B are consistent with this picture, showing that an increase in P3HT covering on the tetrapods results in smaller photocurrents. Finally, the data reveal a complementary trend in the open circuit voltage, which increases with increased coating of the tetrapods. Direct contact of the CdTe to

both electrodes results in shunting, which is mitigated by a thin overlayer of P3HT. Indeed, the open circuit voltage saturates when the tetrapods are completely covered.

While this approach currently allows for sensitive control over blend morphology and subsequent device behavior, the performance of cells described here remains extremely low. It is useful to examine the reasons for low performance, as several factors may contribute and must be considered for future design.

In terms of materials selection and design, the CdTe/P3HT system is expected to perform at least as well as CdSe/P3HT; however, prior studies have shown poor results in the CdTe/P3HT system. CdTe's absorption is better matched to the solar spectrum, but while charge transfer characteristics appear favorable, the reduced energetic driving force for charge transfer may significantly reduce the efficiency of this step. Other critical materials

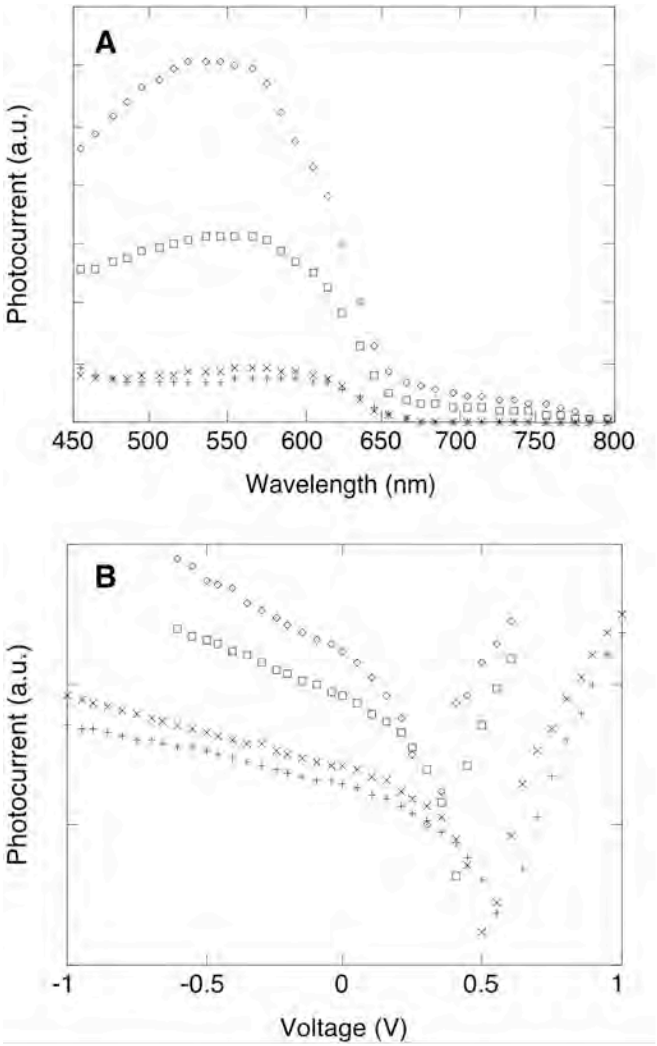

Figure 3.4: Normalized photoaction spectra (**A**) and current-voltage characteristics (**B**) of devices produced from ordered composites show a systematic dependence of photocurrent and open circuit voltage on controlled parameters such as P3HT thickness and electrode contact. Devices depicted in Fig 3.3 (**B-E**) are represented by ◇, □, ×. And + respectively. 100 nm Al was used as a top electrode.

issue could be an increased density of surface traps in CdTe, resulting from differences in surfactant passivation and exchange. We find heuristically that replacement of phosphonic acids and phosphine oxides from the surface of CdTe nanocrystals occurs much more readily than in the CdSe system, potentially indicating that passivation by coordinating ligands is less effective.

In terms of device design, several potential issues may limit the performance of the ordered composite cells described here. The bifunctional ligands employed to bind tetrapods to the ITO surface are designed to be insulating, providing a self-assembled blocking layer to prevent electrons from flowing into the cathode. It is possible, however, that the large van der waals force pressing the tetrapods to the surface of the ITO brings them into electrical contact nonetheless. Significant leakage current is indeed observed at low P3HT loadings. Similarly, the excess binding agent on the ITO surface may act as a blocking layer for hole transport to the cathode, which could account for the low quantum efficiencies that these devices exhibit (<5%). Further research is necessary to understand fully the effects of these issues.

Perhaps the most significant limitation of this system as demonstrated concerns the loading of CdTe in the active blend. While the 3-D tetrapods allow for favorable transport geometries, these structures are very open in space and do not pack well. As the illustrations above show, only low packing densities of CdTe can be achieved via binding to a substrate, even if several monolayers are employed. The result of low CdTe loading is clearly evident in the absorption and EQE spectral response of these devices, which are clearly dominated by P3HT. Absorption is clearly compromised by low CdTe loading

densities, but perhaps more important is the consequential reduction in charge separation efficiency due to an insufficiently distributed heterojunction.

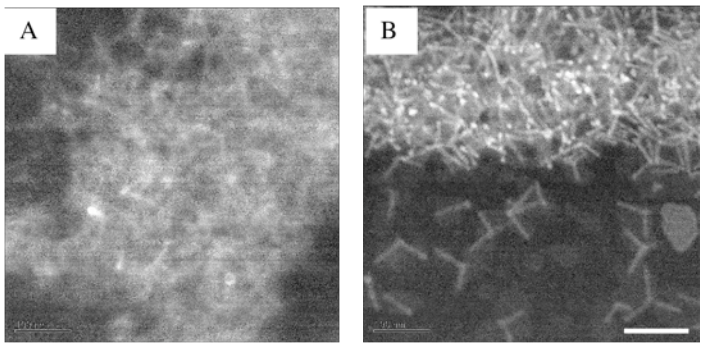

Figure 3.5: Scanning electron micrographs of spin-cast tetrapod array coated with P3HT (**A**) and backside of same film after dissolution of NaC l substrate (**B**). In regions of dense CdTe loading, P3HT does not penetrate entirely to contact substrate. Scale, 100nm.

Increased CdTe loading can be achieved by spincasting tetrapods on the cell surface, as described above; however, penetration of such dense tetrapod arrays with P3HT is not entirely effective. Figure 3.5A shows a scanning electron micrograph of an array of CdTe tetrapods that had been spun-cast on an NaCl tablet, and subsequently covered with P3HT as described above. After dissolving the substrate in water, the backside of the film could be exposed and imaged, as shown in Figure 3.5B. The images seem to indicate a large degree of penetration by P3HT; however, the tetrapod arms are clearly not fully covered in regions of dense CdTe loading. The extent to which P3HT could make contact with the substrate (bottom electrode) is unclear from this image. An alterative approach was also devised, in which a P3HT layer was deposited on an ITO/PEDOT substrate and a

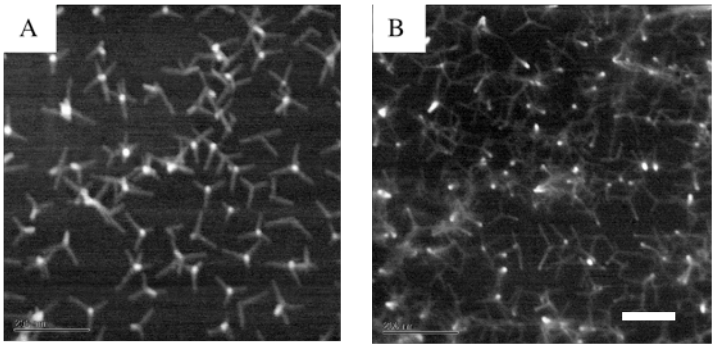

Figure 3.6: Scanning electron micrographs of P3HT film coated with spin-cast tetrapod array, before (**A**) and after (**B**) anneal at 200 °C for 60 mintues in intert atmosphere. Scale, 100nm.

layer of CdTe tetrapods was then deposited on top. Heating the bilayer structure at 200 °C for 30 minutes to an hour caused the tetrapods to be incorporated into the P3HT matrix (Figure 3.6). This is a rather elegant approach, as the resulting structure contains both appropriate and effective contact to electrodes, as well as a separation of the two phases that may allow for an increased diffusional driving force for carrier extraction (*15*).

3.4 Conclusion

The approaches to fabrication of nanocomposite solar cells described here offer several potential advantages over those fabricated by random co-deposition: the particles are naturally aligned toward the electrodes, loading and dispersion are easily controlled and characterized, the organic and inorganic phases are deposited from their preferred solvents rather than a suboptimal co-solution, and exposure of the nanocrystals phase to the top electrode can be controlled. At this early stage, the efficiency of these devices remains rather low, suggesting that further variations of composition, morphology, and annealing are needed. The morphology and efficiency may be improved by using 3-dimensional nanoparticles with greater degrees of branching, thereby better filling space in the device while retaining a well-ordered system(*18*). The next chapter will describe hybrid solar cells based on these 3-d hyperbranched nanocrystals, which fully realize the potential to achieve ordered and highly controlled morphologies in spin-cast bulk-heterojunction solar cells.

References and notes

1. S. E. Shaheen, D. S. Ginley, G. E. Jabbour, *Mrs Bulletin* **30**, 10 (JAN, 2005).
2. B. A. Gregg, M. C. Hanna, *Journal of Applied Physics* **93**, 3605 (MAR 15, 2003).
3. J. J. M. Halls *et al.*, *Nature* **376**, 498 (AUG 10, 1995).
4. G. Yu, J. Gao, J. C. Hummelen, F. Wudl, A. J. Heeger, *Science* **270**, 1789 (DEC 15, 1995).
5. W. L. Ma, C. Y. Yang, X. Gong, K. Lee, A. J. Heeger, *Advanced Functional Materials* **15**, 1617 (Oct, 2005).
6. D. Chirvase, J. Parisi, J. C. Hummelen, V. Dyakonov, *Nanotechnology* **15**, 1317 (Sep, 2004).
7. H. Hoppe *et al.*, *Advanced Functional Materials* **14**, 1005 (Oct, 2004).
8. H. Hoppe, N. S. Sariciftci, *Journal of Materials Chemistry* **16**, 45 (2006).
9. P. K. Watkins, A. B. Walker, G. L. B. Verschoor, *Nano Letters* **5**, 1814 (Sep, 2005).
10. K. M. Coakley, M. D. McGehee, *Applied Physics Letters* **83**, 3380 (OCT 20, 2003).
11. W. U. Huynh, J. J. Dittmer, W. C. Libby, G. L. Whiting, A. P. Alivisatos, *Advanced Functional Materials* **13**, 73 (Jan, 2003).
12. W. U. Huynh, J. J. Dittmer, A. P. Alivisatos, *Science* **295**, 2425 (MAR 29, 2002).
13. D. J. Milliron, I. Gur, A. P. Alivisatos, *Mrs Bulletin* **30**, 41 (JAN, 2005).
14. J. S. Liu, T. Tanaka, K. Sivula, A. P. Alivisatos, J. M. J. Frechet, *Journal of the American Chemical Society* **126**, 6550 (Jun 2, 2004).
15. B. Q. Sun, H. J. Snaith, A. S. Dhoot, S. Westenhoff, N. C. Greenham, *Journal of Applied Physics* **97** (JAN 1, 2005).
16. L. Manna, D. J. Milliron, A. Meisel, E. C. Scher, A. P. Alivisatos, *Nature Materials* **2**, 382 (JUN, 2003).
17. H. T. Liu, A. P. Alivisatos, *Nano Letters* **4**, 2397 (Dec, 2004).
18. A. G. Kanaras, C. Sonnichsen, H. T. Liu, A. P. Alivisatos, *Nano Letters* **5**, 2164 (Nov, 2005).

Chapter 4

Hybrid solar cells with 3-dimensional hyperbranched nanocrystals

4.1 Introduction

Early research in organic photovoltaic systems clearly demonstrated that excitons in conjugated polymers are best harvested via charge separation across a type II donor-acceptor (D-A) heterojunction with another material (*1*). A variety of species - most notably small organic molecules (*2*), other polymers (*3, 4*), C_{60} (*5, 6*), and inorganic semiconductor nanocrystals (*7-11*) - have since been used successfully with conjugated polymers in D-A nanocomposite solar cells. The short exciton diffusion lengths of most conjugated polymers require that these devices be based on a nanoscale composite active layer with a blended or bulk heterojunction (*3, 4*). The morphology of this nanocomposite layer strongly dictates the cells' performance. Polymer domains must be limited in dimension to twice the exciton diffusion length, typically 5-20 nm (*12, 13*), for efficient exciton separation. In addition, both the donor and acceptor phases must form high-quality percolation networks spanning the thickness of the device to ensure efficient carrier collection at the electrodes. Governed by such stringent morphology requirements, processing of nanocomposite D-A heterojunctions is extremely difficult and has been the source of much research (*6, 14-17*).

Constraints on morphology are especially challenging in hybrid nanocrystal-polymer blends (*18, 19*). The most efficient hybrid blends are currently prepared by spin-casting a co-solution of nanocrystals and polymer from a two-solvent system. This process is far from optimal, as dispersion in the solvent relies on metastable solubility of the blend components. The resulting spin-cast film consists of a disordered blend whose specific morphology may vary based on differences in nanocrystal synthesis conditions and cleaning procedures. In addition, small variations in the solvent composition can cause large-scale aggregation of either blend component, with detrimental effects on device performance. Use of nanorods and small, branched nanoparticles has enhanced the performance of polymer-nanocrystal solar cells in recent years (*7, 8, 20, 21*), allowing for improved electron transport vis-à-vis quantum dots. However, electron extraction is still limited in these devices by hopping through a percolation network of particles (*22*). Moreover, the creation of percolation networks in these cells remains highly sensitive to solubility in the blend solutions, and morphological defects and deficiencies are common. Attempts to prescribe the morphology of hybrid blends using ordered templates are promising, but these designs require more complex fabrication methods and have yet to produce significant results (*23, 24*). This work introduces a class of efficient hybrid solar cells whose blend morphology is insensitive to solubility and processing variations, for it is controlled entirely by the 3-D structure of a hyperbranched nanocrystal phase. These cells combine the simple processing and easy fabrication of nanocrystal blend cells with the ordered morphology and transport network of template-based systems.

We recently reported a synthetic method for the creation of 3-D dendritic inorganic nanocrystals with controlled size and branching structure (*25*). As illustrated in

Figure 4.1, these hyperbranched nanocrystals allow the creation of a new class of hybrid solar cells, whose unique architecture affords several advantages over conventional approaches. The branching structure of the nanocrystals controls the dispersion of the inorganic phase in the polymer matrix, thus ensuring a large, distributed surface area for charge separation. Moreover, each hyperbranched particle spans the entire device thickness, and thus contains a built-in percolation pathway for hopping-free transport of electrons to the anode. With decreased sensitivity to variations in processing, a simple monolayer of such nanocrystals in a polymer matrix provides a controlled, ordered, and

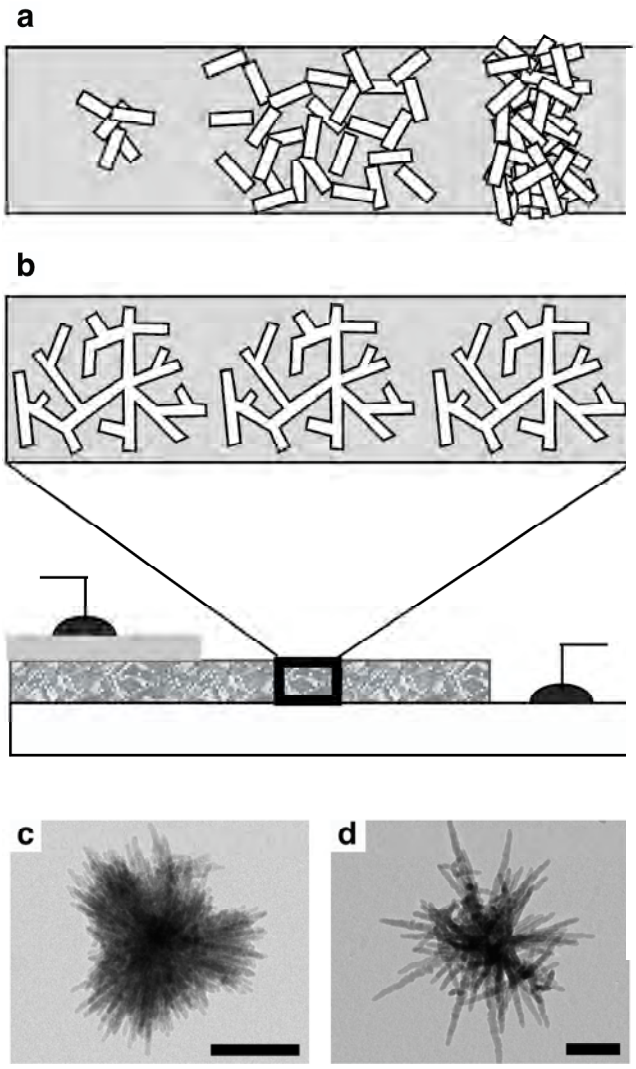

Figure 4.1: A schematic juxtaposes the cross-sectional morphology of traditional hybrid nanocrystal-polymer solar cells (**a**) with that of hybrid devices based on complex hyperbranched nanocrystals (**b**). Defects such as islands and aggregates detrimental to the performance of conventional hybrid cells are eliminated in hyperbranched particle composites, where blend morphology is dictated entirely by the 3-D structure of the hyperbranched nanocrystal. Moreover, the hyperbranched particles span the entire thickness of the active film, thereby enhancing electron transport and eliminating the need for strict control of particle dispersion within the matrix. In **c** and **d**, transmission electron micrographs show the 3-D structure of CdSe and CdTe hyperbranched nanocrystals, respectively. Scale bar, 100nm.

well-defined bulk heterojunction with the dispersion and percolation required for charge separation and transport. Figure 4.1 presents transmission electron micrographs of typical hyperbranched nanocrystals of cadmium selenide (CdSe) and cadmium telluride (CdTe). In this study, hyperbranched CdSe crystals as shown in Figure 4.1c were integrated into a matrix of poly(3-hexylthiophene) (P3HT) to produce hybrid solar cells. The CdSe/P3HT donor-acceptor pair is well understood, and thus serves as a model system for this investigation.

4.2 Synthetic control of branching in coilloidal nanocrystals

As previously documented by our group (*26, 27*), polytypism in cadmium telluride allows for the formation of branch points in a growing nanocrystal. A region of zincblend stacking within an otherwise wurtzite crystallite offers three additional growth trajectories off of the tetragonal close-packed {111} facets, producing in the simplest case a tetrapod nanocrystal. Branching need not occur only at the nucleus of a crystallite; it may also be prompted in situ by thermodynamic or kinetic drivers (*28*). This dissertation focuses predominantly on the use of inorganic nanocrystals in PV devices; however, it is appropriate at this point to share some synthetic results, as synthesizing the correct nanostructure is paramount to creating a controlled and well-defined device.

Given a need to reproducibly synthesize CdTe rods, tetrapods, and hyperbranched particles for the various devices presented here, a comprehensive test was executed to isolate the effects of various synthetic parameters on particle growth. The most illuminating of these experiments involved modifying the nature of alkylphosphonic

acids employed in the synthesis. These molecules are thought to selectively stabilize the non-polar lateral facets of hexagonal CdSe and CdTe nanocrystals (*29*), drastically affecting the kinetic driving force for branching during crystal growth. In Figure 4.2, we show that by modifying the length of the alkyl chain, one can dramatically vary the ultimate shape of synthesized nanocrystals. In CdTe, longer chained phosphonic acids (ODPA, TDPA) were ineffective in promoting any anisotropy at all, while increasingly smaller chained molecules were able to promote the growth of nanorods (OPA), nano-tetrapods (HPA), and higher order branched structures (PPA). In addition, varying the relative amount of a short-chained phosphonic acid in the reaction mixture afforded additional control over anisotropy and branching. Figure 4.3 shows the results of syntheses employing hexylphosphonic acid and octadecyl phosphonic acid, in varying ratios. With no hexylphosphonic acid, isotropic crystals were formed; however, increasing the relative molar concentration of HPA allowed for the formation again of nanorods (20% HPA), nano-tetrapods (40% HPA), and higher order branched structures (>50% HPA).

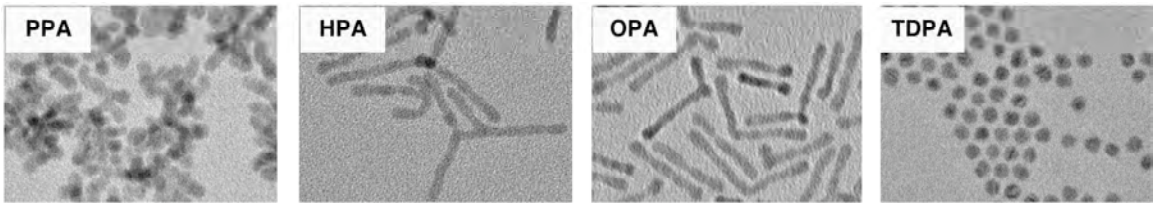

Figure 4.2: Effects of surfactant chain length on anisotropy and branching in CdTe nanocrystals. Syntheses shown utilized 40 % by mol of the surfactant shown.

This experiment illustrated the degree of control afforded by selecting the lengths and relative concentrations of phosphonic acids employed in nanocrystal synthesis. Other members of our group were able to extend these ideas, and proceeded to explore the effect of the specific functionality of this group. By introducing a bifunctional ligand,

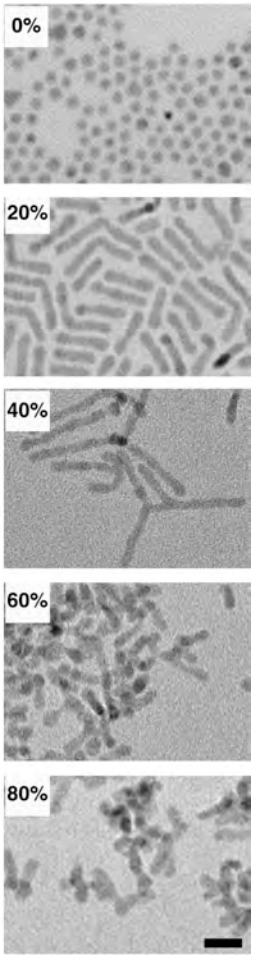

Figure 4.3: Effects of increasing molar concentration of hexylphosphonic acid in synthetic mixture on anisotropy and branching in CdTe nanocrystals

carboxyethyl phosphonic acid, into the standard reaction mixture, they were able to fully realize the potential of higher order branching in these systems. The resulting hyperbranched nanocrystals, described in detail elsewhere (*25*), serve as the basis for a new class of structured bulk-heterojunction solar cells, as discussed in the remainder of this chapter.

4.3 Hybrid composites and bulk heterojunction solar cells based on hyperbranched nanocrystals

In order to explore the advantages of hyperbranched particles and the importance of their pre-formed percolation networks, we present a controlled comparison between nanorod-polymer solar cells and hyperbranched nanocrystal-polymer solar cells, in which the percent of inorganic component is the same. Transmission electron micrographs of these nanocomposite films are shown in Figure 4.4, for six different concentrations of CdSe. The images elucidate several critical differences. With increased loading, nanorods incorporate into the polymer matrix in a random manner, barely occupying some regions while forming large, disordered aggregates in others. In contrast, the hyperbranched particles populate the polymer matrix more deterministically. Similar in dimension to the

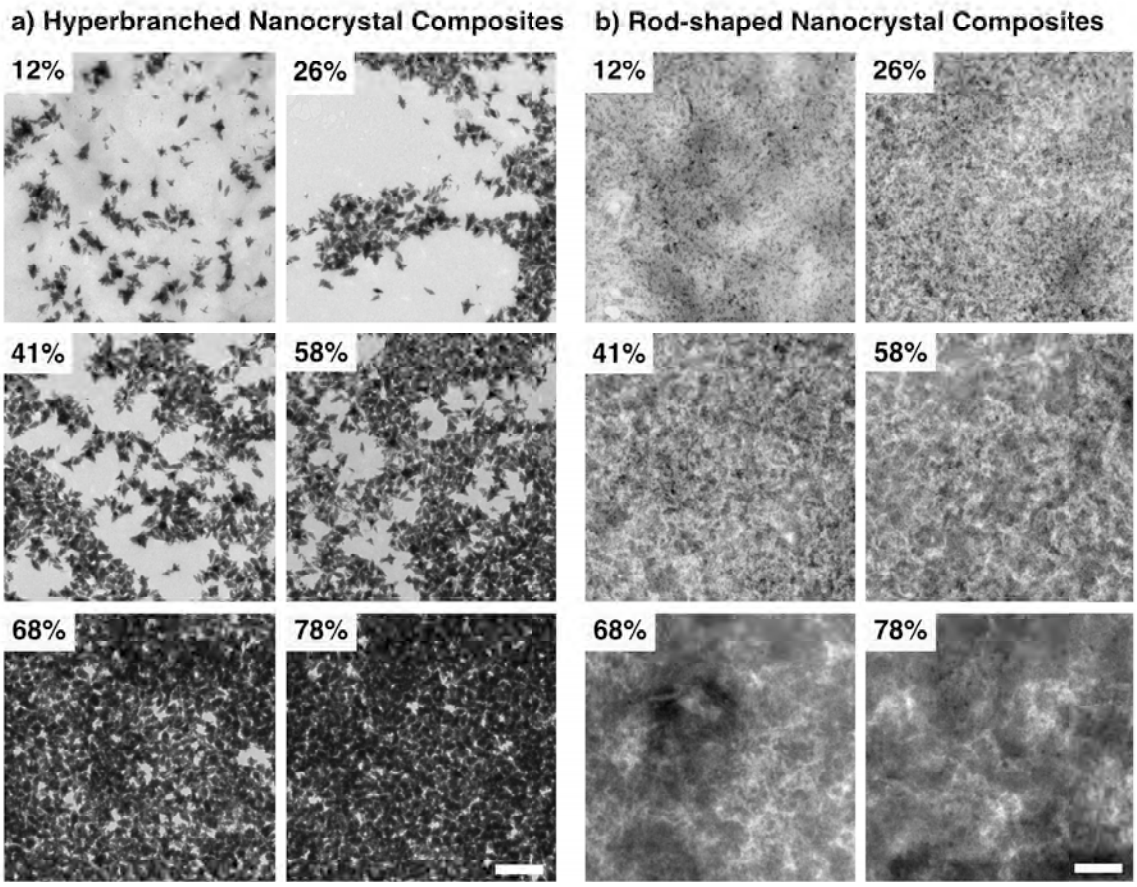

Figure 4.4: Transmission electron micrographs illustrate morphologies of hybrid blends employing hyperbranched nanocrystals (**a**) alongside those composed of nanorods (**b**) at a variety of loading densities. Loading percentages represent concentration of CdSe in spin-casting solution by volume. Scale bar, 500nm.

thickness of the film, they are added contiguously, gradually approaching a well-defined monolayer with increased loading. Moreover, the isotropic shape of the hyperbranched particles eliminates disorder stemming from differences in rotational orientation of the particles. Beyond these geometrical considerations, one must keep in mind the processing differences between the two types of blends. Like organic dendrimers, hyperbranched nanocrystals are more easily processed from fine suspensions without aggregating (*30*). Composites based on these 3-D particles can therefore be spin-cast from a single solvent, and are thus not prone to the large-scale aggregation characteristic

of nanorod blends, which must be spun from a 2-solvent solution. Moreover, processing from a single solvent eliminates the long-range thickness variations of the P3HT matrix. Finally, spin-casting the final blend from pure chloroform, a good solvent for P3HT, should allow for optimal crystallization of polymer domains in the final film.

The differences in morphology and dispersion between rod and hyperbranched nanocrystal composites manifest themselves in the operation of solar cells based on these separate systems. Solar cells based on both sets of composites illustrated in Figure 4.4 were prepared to demonstrate the advantages afforded by hyperbranched particles. Figure 4.5 presents a summary of operating characteristics for these cells, measured under simulated one-sun AM1.5 global illumination. Data points represent highest measured values from a set of 8 regions of each substrate. Cells based on nanorods behave as previously observed. The nominal open circuit voltage (V_{oc}) of a P3HT-only device is measured at low nanorod loading, and is preserved until a threshold representing the formation of CdSe percolation networks across the device is reached (Fig. 4.5a). At this point, the V_{oc} rises to approach that of the complete heterojunction. A similar trend is observed in the short circuit current (J_{sc}) (Fig. 4.5b). Almost no carriers can be extracted from the device at low loading; only when percolation networks begin to form in the nanocrystal phase can charge be extracted from the film.

Cells based on hyperbranched particles exhibit characteristically different behavior. With incorporation of only a small number of nanocrystals, the V_{oc} immediately rises to its full value of approximately 0.6 V, and remains constant with increased loading. That the device behaves like a complete heterojunction with so few particles is easily understood; each hyperbranched particle contains a pre-formed percolation path and can thus fully contribute to photovoltaic conversion. The absence of a threshold loading density is also evident in the J_{sc} of hyperbranched cells, as well as in the final power conversion efficiency (η) (Fig. 4.5d). In contrast with nanorod devices, cells based on hyperbranched particles show a near-linear rise in both I_{sc} and η with increased loading of CdSe. This, too, is consistent with the idea that a single incorporated hyperbranched particle can contribute independently to the cell's output by virtue of its unique morphology.

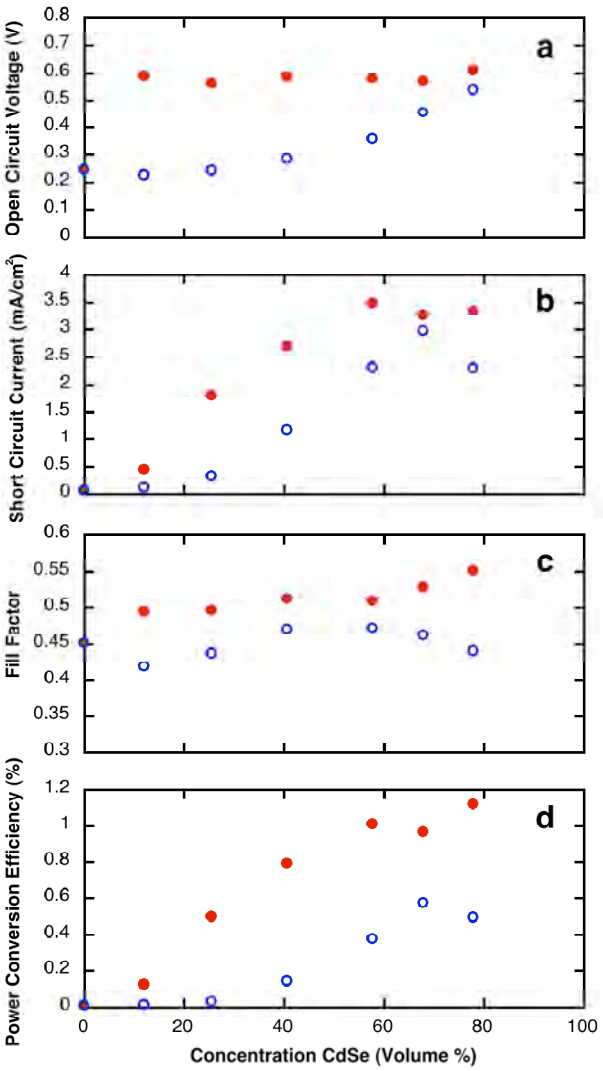

Figure 4.5: Device characteristics for cells based on the blends shown in Fig. 2 elucidate fundamental differences between the operation of hyperbranched nanocrystal (solid circle, red) and nanorod (open circle, blue) solar cells. Data points represent highest measured values from a set of 8 regions of each substrate.

4.4 Built-in percolation of hyperbranched nanocrystal solar cells

In order to validate this model and ensure that the disparate device behavior illustrated in Figure 4.5 does in fact stem from a fundamental difference in percolation behavior of rod and hyperbranched nanocrystals, we performed a spectral analysis of the current output in these cells. Figure 4.6 presents photocurrent spectra from the rod (Fig. 4.6a) and hyperbranched particle (Fig. 4.6b) devices discussed above. The spectral response of pure P3HT, included for reference, is consistent with a measured absorption edge of 660 nm, beyond which the polymer is unable to absorb incident radiation. Any response from blend devices at wavelengths greater than 660 nm must therefore be the direct result of absorption events in the nanocrystalline phase. Thus, the relative current contribution from this low-energy portion of a given spectrum directly reflects the degree to which carriers created in the CdSe are extracted from the device. Accordingly, we define a shape parameter, S, to be the integrated current from 660nm-750nm divided by the fully integrated photocurrent of the cell. Simply put, S is a measure of the cell's ability to extract charges created in the nanocrystals. Fig. 4.6c plots S as a function of CdSe loading for both nanorod and hyperbranched particle cells. The result is clear: a threshold concentration of CdSe is required to allow for the extraction of charges from nan orod CdSe. In contrast, hyperbranched CdSe particles can independently contribute to current generation, even at low concentrations, due to their intrinsically percolated structure.

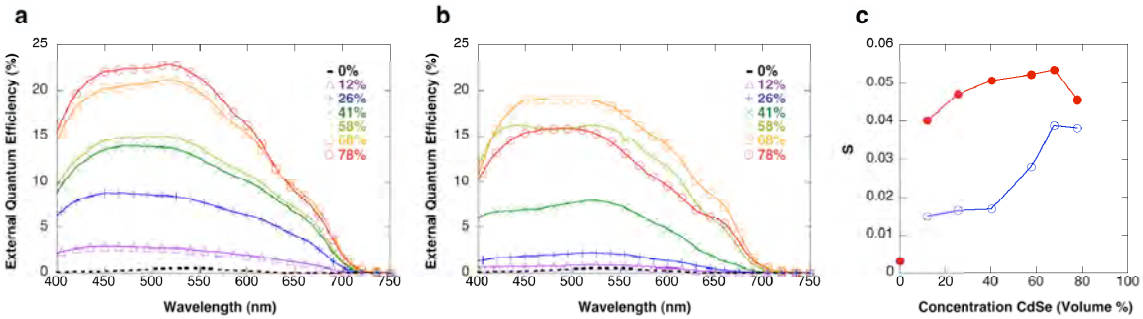

Figure 4.6: Photocurrent spectra of hybrid cells based on hyperbranched-particles (**a**) and nanorods (**b**) are compared. Parameter S is derived from these plots to reflect contribution to the photocurrent exclusively as a result of CdSe absorption events. A plot of S vs. loading density for nanorod (open circle, blue) and hyperbranched nanocrystal (solid circle, red) solar cells elucidates the self-contained percolation structure of hyperbranched nanocrystals.

Note: $$S = \frac{\int_{660nm}^{750nm} EQE(\lambda) \bullet d\lambda}{\int_{350nm}^{750nm} EQE(\lambda) \bullet d\lambda}$$

4.5 Toward optimizing the efficiency of hyperbranched nanocrystal solar cells

A simple model of the hyperbranched nanocrystal solar cell emerges from the analysis above. Each hyperbranched particle embedded within the P3HT matrix represents a very small (roughly 150nm x 150nm x 150nm), yet fully functional hybrid solar cell. These independent single-particle cells are then effectively connected in parallel to create the full device. Data from hyperbranched particle cells support this picture of a simple parallel circuit: voltage remains constant with the addition of hyperbranched particles to the matrix, while the current is additive.

Based on this model, a well-defined, closed-packed monolayer of hyperbranched nanocrystals should yield the highest performance. This is indeed what the experiment shows. Increased CdSe loading in hyperbranched particle cells initially yields a nearly

linear enhancement of power conversion efficiency, but this improvement saturates at high loading concentrations (Fig. 4.5d). Juxtaposed with the TEM images in Figure 4.4 the device data show that cell performance levels off approximately when the hyperbranched particles form a complete monolayer within the P3HT matrix. Beyond a monolayer, additional hyperbranched particles are either excluded from integration into the matrix or, if incorporated, do not appear to have a dramatic effect on performance. Thus, the optimization of hyperbranched particle cells proves simple, well defined, clearly characterized, and easily attained.

Though more easily fabricated, hyperbranched nanocrystal devices outperformed those made from nanorods in every parameter across all measured loading concentrations. Better performing nanorod cells have been reported, but achieving high performance is contingent upon hitting a 'sweet spot' in blend morphology, a difficult task given the system's erratic dependence on particular processing conditions. In contrast, the simple composite architecture of hyperbranched particle cells affords a decreased sensitivity to small variations in loading concentration and processing. This is evident in a comparison of fill factor (FF) parameter between the two classes of devices. FF values, which reflect diode ideality and overall cell quality, are not only higher but much more constant in hyperbranched particle cells than nanorod cells across the range of loading ratios (Fig. 4.5c).

The ability to prescribe dispersion and percolation characteristics of a composite device through choice of nanoparticle structure is perhaps the clearest advantage of hyperbranched nanocrystal solar cells over other hybrid architectures. Still, the efficiencies cited here suggest that the CdSe nanocrystals used in this study are far from

optimal. The specific hyperbranched nanocrystals described here have yielded cells with one-sun AM1.5G efficiencies as high as 2.2%, achieved via optimization of the deposition solvents and the annealing conditions. Figure 4.7 presents current-voltage characteristics for the highest efficiency device to date, alongside a high-magnification TEM image of the composite used to make the cell. Close examination of the blend micrograph reveals that nearly optimal 5nm - 20nm P3HT domains are created between adjacent particles as a result of their urchin-like branching structure. Unfortunately, there appears to be little room for polymer to penetrate the branches of the individual nanocrystals, which would allow significantly more opportunity for efficient charge generation and collection. This suboptimal dispersion poses a synthetic challenge to create more open branching networks in hyperbranched CdSe nanoparticles. Future investigation of specific variations in branching structure on cell performance will help reveal the full potential of this approach, which holds great promise to enable simple fabrication of low cost, high efficiency hybrid solar cells.

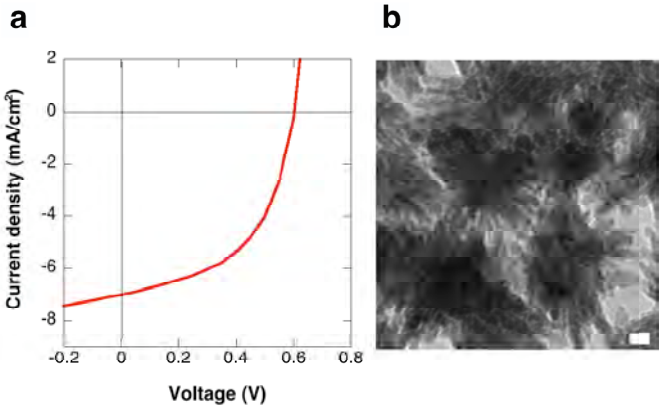

Figure 4.7: Current-voltage characteristics for a hyperbranched nanocrystal cell with a one-sun AM1.5G efficiency of 2.18% (**a**) is presented alongside a TEM micrograph illustrating detailed morphology of this blend (**b**). Cell presented here are limited in performance by the tight branching in these prototype hyperbranched particles. Scale bar, 20nm.

4.6 Conclusion

We have demonstrated a novel architecture for hybrid nanocrystal-polymer solar cells, in which the internal 3-D structure of dentritic inorganic nanocrystals controls nanoscale blending and morphology in the active PV layer. By addressing morphology directly in the nanoparticle design, rather than the solution processing, the resulting devices offer significant practical advantages in fabrication and processing as compared to conventional hybrid organic-inorganic composite solar cells. Moreover, these solar cells have distinct operating characteristics, demonstrating a clear enhancement in carrier extraction stemming from the built-in percolation of hyperbranched particles.

Supplemental methodology

I. Materials. Cadmium oxide (CdO, 99.99+ %), Selenium (Se, 99.999% 100 mesh), tri-*n*-octylphosphine oxide (TOPO, 99 %), and 2-Carboxyethylphosphonic acid (CEPA, 94%) were purchased from Aldrich. *n*-Tetradecylphosphonic acid (TDPA, 99%) and *n*-Hexylphosphonic acid (HPA, 99%) were purchased from PolyCarbon Industries, Inc. Trioctylphosphine (TOP, 97 %) was purchased from Strem Chemicals. Regioregular electronics grade poly(3-hexylthiophene-2,5-diyl) (P3HT) was purchased from Reike Specialty Polymers. All solvents used were anhydrous, purchased from Aldrich, and used without any further purification.

II. Synthesis of CdSe nanorods and hyperbranched particles. All manipulations were performed using standard air-free techniques. In a typical synthesis of CdSe hyperbranched particles [nanorods], a mixture of 1.00 g TDPA, 50 mg CEPA, 3.00 g TOPO, and 155 mg CdO [710 mg TDPA, 160 mg HPA, 3.00 g TOPO, and 200 mg CdO] was degassed at 120 ºC for 60 minutes in a 25 ml three-neck flask connected to a Liebig condenser. It was heated slowly under Ar until the CdO decomposed and the solution turned clear and colorless. Next, 1.2 g of TOP [1.5 g of TOP] were added, and the temperature was further raised to 315 ºC [300 ºC]. A stock solution of Se dissolved in TOP at 3.1% [15%] Se by weight was previously prepared, and 0.3 g [0.489 g] were rapidly injected to the vigorously stirring precursors and particles were allowed to grow for 15 minutes [5 minutes] before the heat was removed to stop the reaction. After cooling the solution to 70 ºC, 3–4 ml anhydrous toluene were added to the flask, and the dispersion was transferred to an Ar drybox. The minimum amount of anhydrous

isopropanol required to precipitate the nanocrystals was added to the dispersion. This prevented potential co-precipitation of the Cd-phosphonate complex. After centrifuging and removing the supernatant, the precipitate was re-dissolved in pure toluene.

III. Device fabrication. All manipulations were performed using standard air-free techniques. To create cells based on hyperbranched nanocrystals [nanorods], particles synthesized as described above were washed 2x by dissolution in toluene and subsequent precipitation with isopropanol, then suspended in 20 mL pyridine and stirred under reflux overnight for comprehensive ligand exchange. After reflux, the nanocrystals were precipitated with hexane, washed with toluene, and re-suspended in approximately 500 μL chloroform [dissolved in approximately 1 mL of a 10% by volume solution of pyridine in chloroform]. These highly concentrated suspensions [solutions] were ultrasonicated for ca. 10 minutes and combined with solutions of P3HT in pure chloroform [in a 10% by volume solution of pyridine in chloform]. The blends were then spin-cast at 1500 rpm onto glass substrates coated with 150 nm ITO (Thin Film Devices Inc., resistivity 20 ohms/sq), and annealed on a hot plate at 120 ºC for 60 minutes. Finally, samples were held at ca. 10^{-6} torr overnight, after which aluminum top electrodes were deposited by thermal evaporation through a shadow mask, resulting in individual devices with 0.03 cm^2 nominal area. The device shown in figure 5 was made using P3HT dissolved in trichlorobenzene rather than chloroform, and was annealed at 150 ºC for 60 minutes after deposition of the top contacts.

IV. Device characterization. Simulated AM1.5G illumination was obtained with a Spectra Physics Oriel 300W Solar Simulator with AM1.5G filter set. The integrated

intensity was set to 100 mW/cm2 using a thermopile radiant power meter (Spectra Physics Oriel, model 70260) with fused silica window, and verified with a Hamamatsu S1787-04 diode. Intensity was controlled to be constant throughout measurements with a digital exposure controller (Spectra Physics Oriel, model 68950). Spectral response curves were measured at low intensity (<0.1 mW/cm2), using monochromated light from a tungsten source.

References and notes

1. C. W. Tang, *Applied Physics Letters* **48**, 183 (JAN 13, 1986).
2. R. A. J. Janssen *et al.*, *Journal of Chemical Physics* **103**, 8840 (Nov 22, 1995).
3. J. J. M. Halls *et al.*, *Nature* **376**, 498 (AUG 10, 1995).
4. G. Yu, A. J. Heeger, *Journal of Applied Physics* **78**, 4510 (1995/10/01/, 1995).
5. G. Yu, J. Gao, J. C. Hummelen, F. Wudl, A. J. Heeger, *Science* **270**, 1789 (DEC 15, 1995).
6. S. E. Shaheen *et al.*, *Applied Physics Letters* **78**, 841 (FEB 5, 2001).
7. W. U. Huynh, J. J. Dittmer, A. P. Alivisatos, *Science* **295**, 2425 (MAR 29, 2002).
8. B. Q. Sun, E. Marx, N. C. Greenham, *Nano Letters* **3**, 961 (Jul, 2003).
9. A. C. Arango, S. A. Carter, P. J. Brock, *Applied Physics Letters* **74**, 1698 (Mar 22, 1999).
10. W. J. E. Beek, M. M. Wienk, M. Kemerink, X. N. Yang, R. A. J. Janssen, *Journal of Physical Chemistry B* **109**, 9505 (May 19, 2005).
11. E. Arici, N. S. Sariciftci, D. Meissner, *Advanced Functional Materials* **13**, 165 (FEB, 2003).
12. J. J. M. Halls, K. Pichler, R. H. Friend, S. C. Moratti, A. B. Holmes, *Applied Physics Letters* **68**, 3120 (1996/05/27/, 1996).
13. T. J. Savenije, J. M. Warman, A. Goossens, *Chemical Physics Letters* **287**, 148 (1998/4/24, 1998).
14. W. L. Ma, C. Y. Yang, X. Gong, K. Lee, A. J. Heeger, *Advanced Functional Materials* **15**, 1617 (Oct, 2005).
15. D. Chirvase, J. Parisi, J. C. Hummelen, V. Dyakonov, *Nanotechnology* **15**, 1317 (Sep, 2004).
16. H. Hoppe *et al.*, *Advanced Functional Materials* **14**, 1005 (Oct, 2004).
17. P. K. Watkins, A. B. Walker, G. L. B. Verschoor, *Nano Letters* **5**, 1814 (Sep, 2005).
18. W. U. Huynh, J. J. Dittmer, W. C. Libby, G. L. Whiting, A. P. Alivisatos, *Advanced Functional Materials* **13**, 73 (Jan, 2003).
19. J. S. Liu, T. Tanaka, K. Sivula, A. P. Alivisatos, J. M. J. Frechet, *Journal of the American Chemical Society* **126**, 6550 (Jun 2, 2004).
20. B. Q. Sun, H. J. Snaith, A. S. Dhoot, S. Westenhoff, N. C. Greenham, *Journal of Applied Physics* **97** (JAN 1, 2005).
21. W. U. Huynh, X. G. Peng, A. P. Alivisatos, *Advanced Materials* **11**, 923 (AUG 3, 1999).
22. N. C. Greenham, X. G. Peng, A. P. Alivisatos, *Physical Review B* **54**, 17628 (Dec 15, 1996).
23. K. M. Coakley, M. D. McGehee, *Applied Physics Letters* **83**, 3380 (OCT 20, 2003).
24. K. M. Coakley, Y. X. Liu, C. Goh, M. D. McGehee, *Mrs Bulletin* **30**, 37 (JAN, 2005).
25. A. G. Kanaras, C. Sonnichsen, H. T. Liu, A. P. Alivisatos, *Nano Letters* **5**, 2164 (Nov, 2005).

26. L. Manna, E. C. Scher, A. P. Alivisatos, *Journal of the American Chemical Society* **122**, 12700 (DEC 27, 2000).
27. L. Manna, D. J. Milliron, A. Meisel, E. C. Scher, A. P. Alivisatos, *Nature Materials* **2**, 382 (JUN, 2003).
28. D. J. Milliron *et al*., *Nature* **430**, 190 (JUL 8, 2004).
29. X. G. Peng *et al*., *Nature* **404**, 59 (MAR 2, 2000).
30. J. M. J. Frechet, *Science* **263**, 1710 (Mar 25, 1994).

Chapter 5

All-inorganic nanocrystal solar cells

5.1 Introduction

In recent years, a well-accepted model has emerged to describe the operation of organic based solar cells and distinguish them from their conventional inorganic counterparts (*1, 2*). The organic donor-acceptor solar cell relies on a type II heterojunction, which serves to dissociate the strongly bound excitons characteristic of organic systems. Materials design for this type of photovoltaic system thus requires proper energy band alignment of active materials to facilitate charge transfer. Examples to date have been limited to systems utilizing at least one active organic component (*3-8*). However, studies of type II semiconductor nanocrystal heterostructures demonstrate that efficient charge transfer may also occur between two such inorganic components with staggered energy levels (*9, 10*). In addition, recent research has revealed a growing number of similarities between films of nanocrystals and organic molecular semiconductors. As is the case with organic systems, nanocrystal films exhibit extremely low carrier concentrations and high trap densities (*11, 12*), as well as strongly confined excitations which may migrate between crystals (*13*). All of these properties are sufficient, and some requisite, for solar energy conversion based on the donor-acceptor model (*1, 2*). The strong similarities between the two classes of materials suggest that a

nanocrystal donor-acceptor solar cell may be constructed without any organic component.

5.2 Design and fabrication

The photovoltaic devices described here utilize rod-shaped cadmium selenide (Figure 5.1A) and cadmium telluride (Figure 5.1B) nanocrystals, synthesized and prepared separately (*21*). A schematic energy diagram in Figure 5.1C illustrates the staggered band alignment of this prototypical donor-acceptor pair (*14*). In fabricating devices, nanocrystals were spin-cast from a filtered pyridine solution, allowing for the creation of ultra thin, flexible films of densely packed nanocrystals on virtually any substrate. In Figure 5.1D, a representative scanning electron micrograph shows that

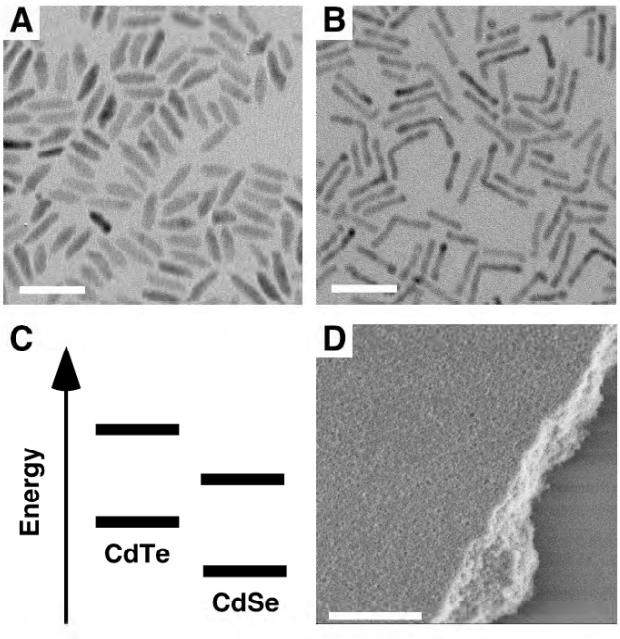

Figure 5.1: Transmission electron micrographs of (**A**) CdSe and (**B**) CdTe nanocrsytals utilized in this investigation. Scale bar, 40 nm. In (**C**), an energy diagram of valence and conduction band levels for CdTe and CdSe illustrates the type II charge-transfer junction formed between the two materials. Employing the effective mass approximation, bulk energy levels were modified to account for quantum confinement. Valence band edges for CdSe and CdTe rods were calculated to be -4.79 eV and - 4.12 eV respectively. Conduction band edges for CdSe and CdTe rods were calculated to be -6.64 eV and -5.85 eV respectively. In (**D**), a typical spin-cast film of colloidal nanocrystals imaged by scanning electron microscopy is homogeneous and defect free; the film edge of this ca. 100 nm film is shown for contrast with the silicon substrate. Scale bar, 1 μm.

typical films are homogeneous and pinhole-free over large areas.

Planar donor-acceptor heterojunctions were fabricated by sequentially spin-casting films of CdTe followed by CdSe on indium tin oxide (ITO) glass. Thermally deposited aluminum was used as a reflective top contact. Brief annealing of the first film for 15 minutes at 200 degrees C was found to remove residual solvent and allow for superjacent deposition of the second film, thus creating high quality bilayer structures with minimal intermixing at the interface (*15*).

In Figure 5.2A, the photoaction spectrum of a typical bilayer cell reveals features from both the CdSe and CdTe absorption spectra, demonstrating that both components contribute to the photocurrent. Current-voltage characteristics of this device in the dark and at simulated AM1.5G full-sun illumination are presented in Figure 5.2B. The device exhibits strong photo-response and diode rectification in the dark and light. In addition,

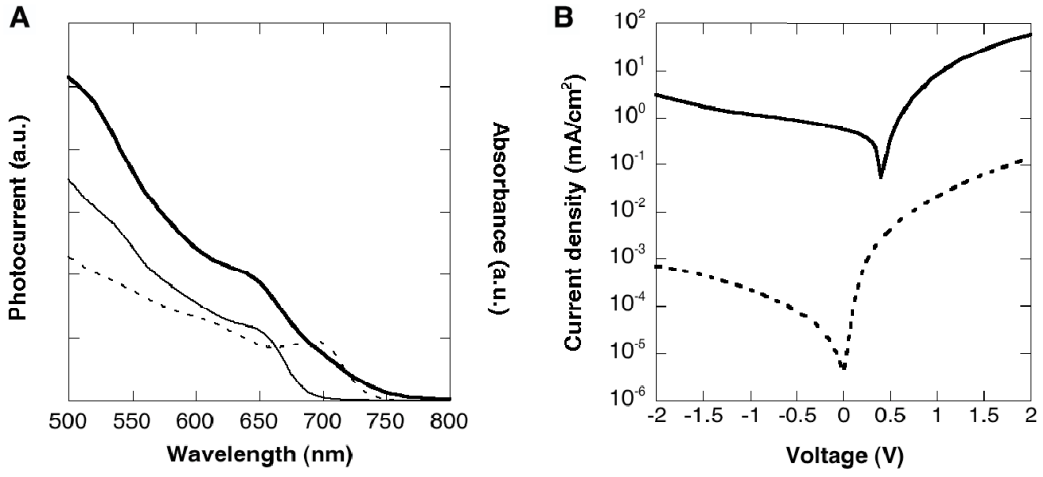

Figure 5.2: (**A**) The normalized photocurrent spectral response of a typical ITO/100 nm CdTe/100 nm CdSe/Al bilayer device (bold) is illustrated alongside solution-phase absorption spectra for the CdTe (dotted) and CdSe (solid) nanocrystals from which the device was fabricated. The photoaction spectrum reflects the red CdTe absorption edge and the prominent CdSe exciton peak, indicating that both components are active. (**B**) Current-voltage characteristics for this device in the dark (dotted) and under simulated one-sun AM1.5G illumination. The device behaves as a rectifying diode with a significant photovoltaic response. Note also the strong photoconductive response of the device.

this representative cell exhibits a significant photovoltaic effect, with short circuit current (I_{sc}) of 0.58 mA/cm^2, open circuit voltage (V_{oc}) of 0.41 V, and fill factor (FF) of 0.40 (*16*).

5.3 Basic operation

5.3.1 Proposed mechanism

Given their ostensibly similar structures, it is necessary to distinguish the solar cells presented here from conventional thin film heterojunction cells. Conventional cells depend on a junction between bulk p- and n- doped materials to form a built-in field, which then acts as the primary driving force for minority carrier extraction (*17, 18*). Similar to organic semiconductors, colloidal nanocrystals are characterized by extremely limited free-carrier concentrations (*19*). In fact, three-dimensional CdSe colloid arrays have been found to contain essentially no free carriers without illumination (*12*). As such, the creation of a depleted junction in these nanocrystal cells is highly unlikely.

In accordance with prior studies, the CdSe and CdTe films presented here are electrically insulating in the dark. Measuring surface conduction across a 1mm gap between two aluminum electrodes yields linear IV curves, from which sheet resistances exceeding 500 G-ohms/□, a value limited by the measurement apparatus, can be extracted for films of either material on glass substrates. Exposing the films to 100 mw/cm2 full-sun irradiation affects a dramatic rise in conductivity. Sheet resistances, now measurable, drop at least one order of magnitude under illumination. Likewise,

illumination affords a greater than three order of magnitude enhancement in conductivity of the device itself, as demonstrated in Figure 5.2B. This strong photoconductive effect suggests that these materials, like their organic counterparts, have an extremely limited number of untrapped carriers in the dark, and are better characterized by a rigid band model than one employing band bending.

Accounting for these effectively undoped active materials, we propose a mechanism for photovoltaic conversion based on donor-acceptor charge transfer. Those photoexcitations that probe the CdTe/CdSe junction experience an energetic driving force for charge transfer, with holes finding lower energy states in the CdTe and electrons finding lower states in the CdSe. Carrier extraction is driven not by means of a built-in field created from a depletion region of substitutional dopants; rather, extraction is primarily driven by directed diffusion, as dictated by the type II heterojunction. After absorption and charge transfer, majority holes in the CdTe readily diffuse into the ITO, but are blocked from moving through the CdSe toward the Al electrode. Likewise, majority electrons in the CdSe can diffuse only toward the Al, and not through the CdTe to the ITO. The well-accepted metal-insulator-metal model, in which electrodes of disparate work function equilibrate to form a field across the dielectric active materials, likely provides an additional driving force for carrier extraction.

5.3.2 Evidence and role of charge transfer

In order to assess the role of charge transfer in facilitating photovoltaic energy conversion, devices comprised of a thin-film of only one nanocrystal material were

juxtaposed with cells containing charge transfer junctions between the two types of crystals. All devices had comparable thicknesses of active materials on the order of 100 nm and comparable optical densities across the spectrum. A direct comparison of external quantum efficiencies in the CdTe-only, CdSe-only, and bilayer CdTe/CdSe devices appears in Figure 5.3, showing a significant enhancement in creation and extraction of carriers due solely to the presence of a charge transfer interface within the device. As is the case in organic systems, separation of electrons and holes across the interface enhances the diffusional driving force for charge extraction while reducing the likelihood of geminate recombination within the system. Results for devices composed of intimately mixed blends of CdSe and CdTe nanocrystals also appear in Figure 5.3. These blend films similarly exhibit enhanced quantum efficiencies over single-material cells, offering further evidence that the photoaction of these devices is based on a donor-acceptor junction rather than a conventional planar p-n junction (*20*).

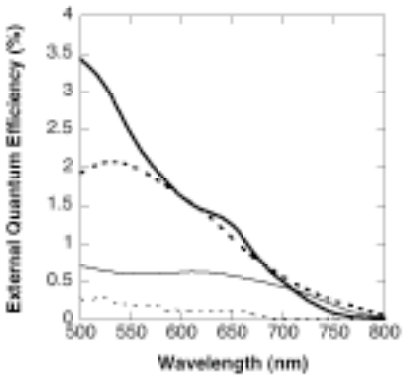

Figure 5.3: A comparison of external quantum efficiency spectra shows significant enhancement in bilayer (bold, solid) and blend (bold, dotted) devices versus a CdTe single-material device (solid) and CdSe single-material device (dotted), all of comparable optical density. The comparison serves to illustrate the role of charge transfer in photocurrent generation.

In traditional donor-acceptor systems, photoluminescence (PL) quenching of one component by the other is generally offered as direct evidence of donor-acceptor charge transfer (*21*). Since the nanocrystals employed here exhibit extremely low photoluminescence quantum yields, especially after surfactant replacement with pyridine, PL quenching is not a viable measure of charge transfer. Instead, ultrafast photo-induced absorption (PIA) spectroscopy was employed to probe carrier states and dynamics in the prototypical CdTe-CdSe system presented above. Figure 5.4 reveals spectrally resolved pump-probe data for the four films described above, consisting of only CdTe (5.4A), only

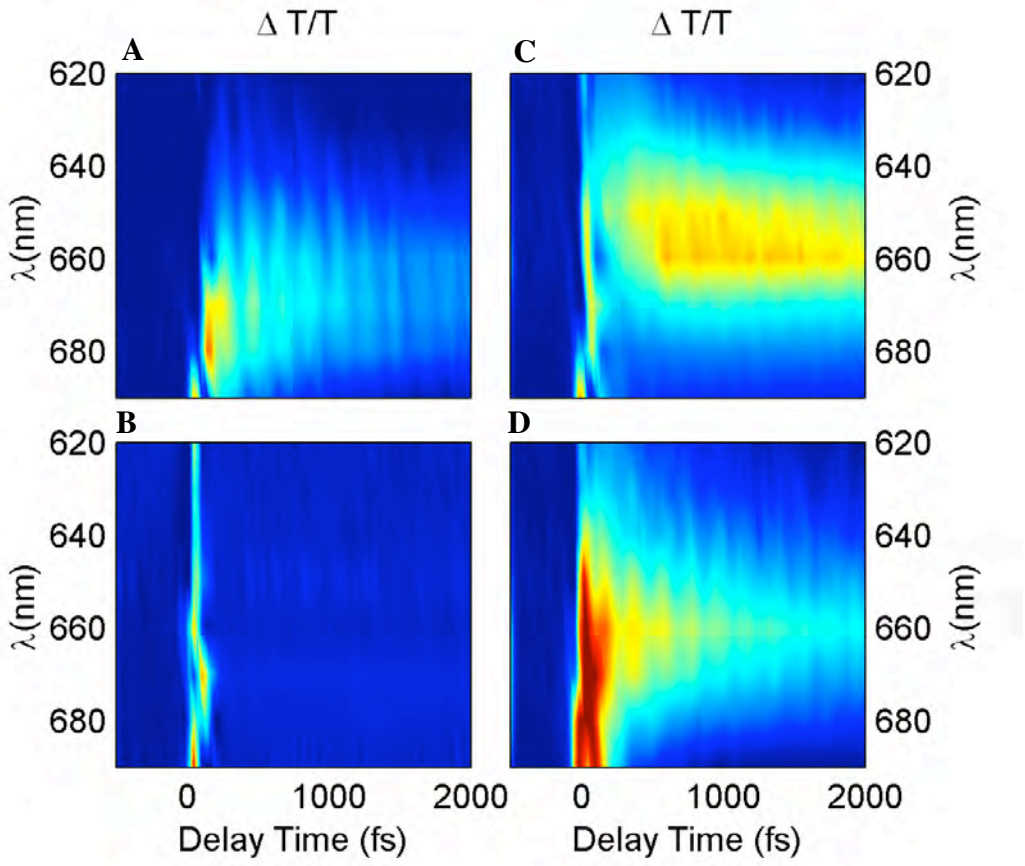

Figure 5.4: Spectrally resolved pump-probe data for a CdTe single-materials (A), CdSe single-material (B), blend (C), and bilayer (D) films, all of comparable optical density. Pumping at 720 nm allows for selective excitation in CdTe. Probing the CdSe band edge reveals strong evidence of charge transfer in blend films, while data in (D) suggests that charge transfer may be limited to the near-junction region in bilayer architectures.

CdSe (5.4B), a blend of the two nanocrystal materials (5.4C), and a nanocrystal CdTe-CdSe bilayer film (5.4D). All samples were excited with 720 nm radiation (10nm FWHM, 30 $\mu J/cm^2$, 250 kHz repetition rate), thereby producing excitations exclusively in the CdTe and not in the CdSe. Probing near the band edge of the CdSe (250 kHz, 100μW) revealed affects of charge transfer in the films that contained both components.

The blend film shows a strong, long-lived bleaching at the band edge of CdSe after excitation of CdTe at t=0, providing strong evidence for a charge transfer event occurring at a sub picosecond rate. In constrast, the CdTe control shows a distinct characteristic signature, with monotonic decay at approximately 670 nm, and, as expected, the CdSe control shows no signal as no excitations have been created. The bilayer sample appears to include features of both the CdTe-only signature and the blend signature, which may indicate that charge transfer only occurs within a narrow interfacial region of these films. Further experimentation and analysis will be required for a more complete understanding of this phenomenon (*22*).

5.3.3 Current-voltage characteristics

Additional information regarding the mechanism for charge extraction can be gained from comparing the current-voltage characteristics of these various devices. It has already been noted that cells based on heterojunction bilayers exhibit good diode behavior with strong rectification. By comparison, current-voltage characterization of devices composed of only CdTe or only CdSe showed no significant rectification. We

can thus deduce that the observed photovoltaic effect in the bilayer is not a result of Schottkey contacts to either material, but rather is due to the intended heterojunction.

Having ruled out the presence of conventional p-n or Shottkey junctions, it appears that the bilayer nanocrystal cell operates by means of the diffusion assisted donor-acceptor heterojunction typical of organic devices. It is important, however, to note several characteristics of the nanocrystal solar cell that set it apart from its organic-based counter parts. Perhaps most striking is the fact that while the most efficient organic solar cells are based on distributed heterojunctions, devices based on simple blends of donor and acceptor nanocrystals (Figure 5.5) neither rectify nor produce a significant photovoltage. This poor performance can be attributed to the fact that, in contrast to organic systems, common electrodes do not readily form selective contacts to either the donor or acceptor nanocrystals. Electrons and holes can be injected into either material, such that blend cells pass current in both forward and reverse bias. Incorporation of blocking layers in future cell designs may allow for further investigation of the blend system.

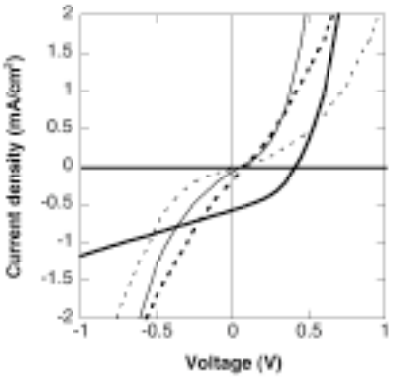

Figure 5.5: A comparison of current-voltage characteristics between the same devices: nearly symmetric current-voltage behavior in the single-material devices suggests that diode behavior in the bilayer is not simply the result of a Schottkey junction with either material. With no contact selectivity, blend cells show negligent rectification and photovoltage at simulated AM1.5G illumination.

5.3.4 Origin of the V_{oc}

As illustrated in Chapter 2, a clear advantage of nanocrystal-based PV designs is the ability to easily tune nanocrystal band gaps through quantum confinement by simply varying crystal dimensions. By the effective mass approximation, a change in bandgap in CdSe or CdTe is manifested as a significantly larger shift in the conduction band edge compared with the resulting shift in the valence band edge. Thus, one can easily vary the electron acceptor strength simply by changing crystal size.

In an effort to provide further insight into the operation of the nanocrystal donor-acceptor cells discussed above, three sets of CdSe nanorods were synthesized with comparable length but varying diameters. In Figure 5.6, absorption spectra for the three syntheses are presented, alongside a schematic illustrating the effect of this band gap variation on CdSe acceptor strength. The crystals, whose band gaps ranged from 1.794 eV to 1.964 eV as a result of the quantum confinement, were integrated into the basic bilayer CdTe/CdSe solar cells described above. Figure 5.7A illustrates the effect of band

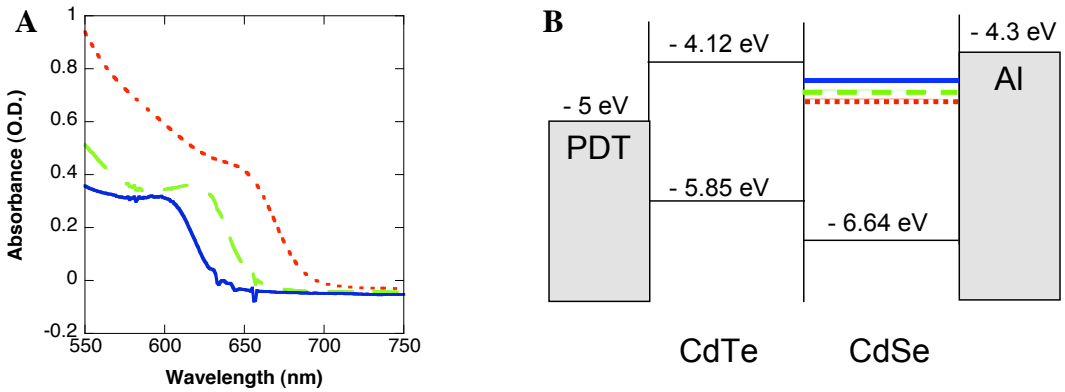

Figure 5.6: Absorption spectra for the product of three syntheses of CdSe, producing particles of decreasing diameter, illustrate the effect of quantum confinement in the system (A). A schematic representation of the resulting conduction band edges of these particles in the context of the energetic structure of a complete CdTe/CdSe nanocrystal solar cell (B).

gap variation in CdSe on the device open-circuit voltage. A linear dependence emerges, with a slope of approximately 0.72. Since the ratio of electron mass to hole mass in CdSe is approximately 0.8, this result suggests a near-direct coupling of open-circuit voltage and acceptor strength, consistent with prior reports on organic donor-acceptor systems (*23, 24*).

Further insight is revealed in comparing these results to those obtained with devices based on blends of CdTe/CdSe, employing the same systematic variation in CdSe band gap. Blend devices were fabricated as described above; however, a roughly 50nm PEDOT layer was added to provide an electron barrier to the ITO electrode and thus allow for appreciable open circuit voltage. Characteristics for these devices (Figure 5.7A) reveal a nearly identical dependence of V_{oc} on band gap and, in turn, acceptor strength to the bilayer system. However, open-circuit voltages for blend devices are a nearly constant 0.2 eV lower than those of bilayer devices for all CdSe sizes. The additional V_{oc} evident in bilayer architectures is attributed to the need to overcome a strong driving force for charge extraction resulting from directed diffusion of carriers away from the planar interface. The additional contribution to the V_{oc} remains constant regardless of acceptor strength. This effect has been predicted and partially observed in the literature (*1, 25*), but the illustration presented here is among the most clear and definite to date.

In addition to acceptor strength, one must consider the effects of electrode work function on built-in-field and open circuit voltage. Bilayer devices were prepared on ITO as described above with calcium, aluminum, and gold top electrodes. As illustrated in Figure 5.7B, no clear dependence of open circuit voltage on electrode work function is observed. This, too, is consistent with prior reports on organic donor-acceptor cells, which attribute the result to a pinning of electrode work function to the conduction band edge of the acceptor material (*24*). Given that a large number of surface states are known to be present in many colloidal nanocrystals systems, this hypothesis is certainly reasonable for the device architectures reported here.

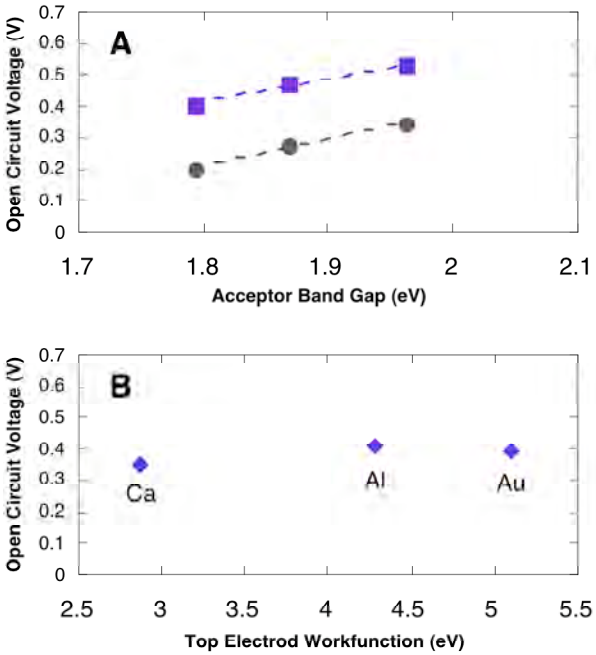

Figure 5.7: (A) illustrates the dependence of open-circuit voltage on acceptor bandgap for bilayer (blue squares) and blend (brown circles) devices. Both exhibit linear dependences with slopes of 0.72 and 0.84 respectively, suggesting a near-1:1 correlation with acceptor strength. Bilayer devices show a constant ~0.2 V higher V_{oc} due to additional diffusion currents. A poor correlation between V_{oc} and electrode work function may be evidence of Fermi-level pinning (B).

5.3.5 Toward enhanced performance

Another fundamental distinction of the nanocrystal system has direct consequences on the performance of these devices. While a heterojunction is nearly

always required to efficiently produce free charges from excitons in organic systems, this is not the case for the nanocrystals utilized in this study. Rod shaped nanocrystals with high aspect ratios exhibit little confinement along the length of the rod (*26*). Excitations can thus dissociate over this dimension, creating free carriers throughout the nanocrystal film. This is a significant departure from organic systems, in which free carriers are created only when otherwise tightly bound excitons are separated across the donor-acceptor junction.

With both free electrons and holes residing in the donor and acceptor materials, carriers are more susceptible to non-geminate recombination in the nanocrystal system. This recombination is compounded by the large presence of surface states on the nanocrystals, which act to trap carriers as they move through the film. Indeed, detrimental recombination losses are apparent in the low quantum efficiency of the nanocrystal cell compared with similar devices made from organic semiconductors.

It is possible to minimize the high surface trap area inherent in a densely packed array of nanocrystals and concurrently improve carrier transport in the device by annealing and sintering the crystals, as illustrated in the following section.

5.4 Sintered nanocrystal solar cells

5.4.1 Basic operation

Following a well-known technique to facilitate sintering of CdTe thin films (*27*), nanocrystal films were exposed to a saturated solution of cadmium chloride in methanol

and annealed at 400 degrees in oxygen for 15 minutes. After sintering, films of CdSe and CdTe remain insulating in the dark, but show an approximately one order of magnitude enhancement in photoconductivity. This suggests that the sintering process dramatically improves carrier transport, but does not result in significant doping. An examination of the sintered films by scanning electron microscopy supports this idea, revealing significant grain growth as illustrated in Figure 5.8.

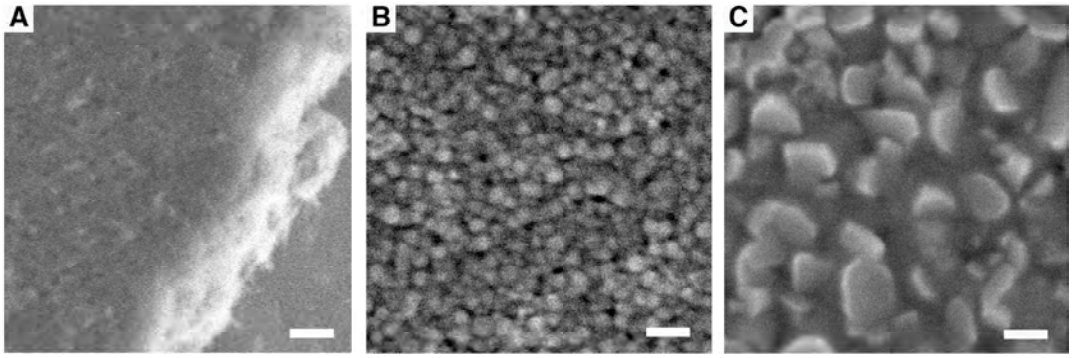

Figure 5.8: In (A), a scanning electron micrograph illustrates the structure of a typical as-deposited nanocrystal film (in this case, a blend of CdSe and CdTe). After exposure to $CdCl_2$ and a 15 minute anneal in air, these nanocrystal films undergo dramatic microstructural change. Sintered nanocrystal films of CdSe (B) and CdTe (C) exhibit recrystallization and significant grain growth. Scale bar, 100 nm.

The photo-response of sintered CdTe/CdSe bilayer cells mirrors the drastic rise in photoconductivity exhibited by the active layers. A typical photoaction spectrum appears in Figure 5.9A, showing external quantum efficiencies approaching 70% (*28*). As expected, the spectrum reflects a strong red-shift in the onset of photocurrent to the bulk absorption edge. With I_{sc} of 11.6 mA/cm^2, V_{oc} of 0.40 V and FF of 0.45, the resulting solar cell demonstrates a power conversion efficiency of 2.1 % under simulated AM1.5G illumination (*29*). Note that the enhancement in efficiency arises solely from the dramatic increase in photo-response, while cells exhibit a nearly unchanged open circuit voltage after sintering (Figure 5.9B). This is strong evidence that the driving force for

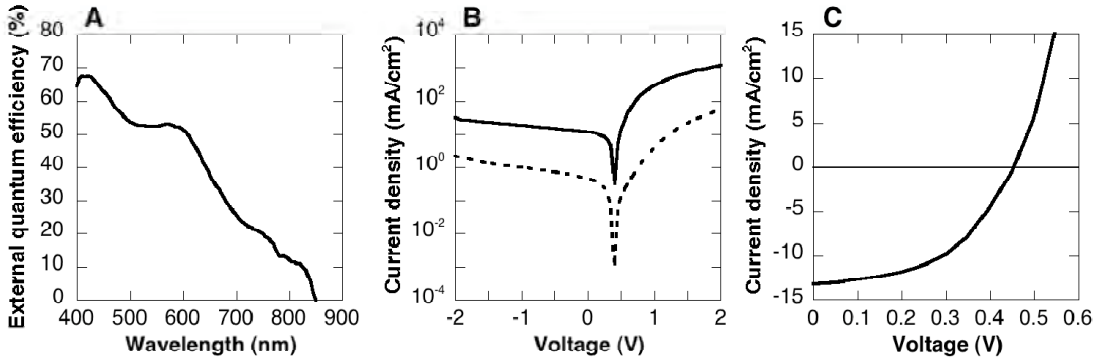

Figure 5.9: (**A**) The normalized photo-action spectrum of a typical bilayer device after sintering reveals the broadened spectral response and enhanced quantum efficiency that result from sintering. (**B**) Current-voltage characteristics of a typical bilayer device before sintering (dotted) and after sintering (solid), measured at simulated one-sun AM1.5G illumination. The sintered cell shows over an order of magnitude enhancement in photocurrent while the open circuit voltage remains virtually unchanged. (**C**) Utilizing a Ca 20nm/Al 80nm top contact allows for fabrication of devices with AM1.5G power conversion efficiencies as high as 2.9%

charge extraction is the same in sintered and unsintered devices. Note also in Figure 5.10 that varying the annealing time after exposure to $CdCl_2$ has a strong effect on device current, but little effect on voltage.

Testing the sintered ITO/HRT/CdSe/CdTe/Al system at high illumination intensities revealed that the open-circuit voltage measured at one-sun does not reflect the full potential of the system. Figure 5.11 shows a near-logarithmic rise in V_{oc} without saturation for intensities up to 20 suns. Higher open-circuit voltage, and higher efficiencies, have also been achieved in sintered nanocrystal cells by varying simple system parameters such as electrode material. Figure 5.9C shows current-voltage characteristics for the best device fabricated to date. Employing a

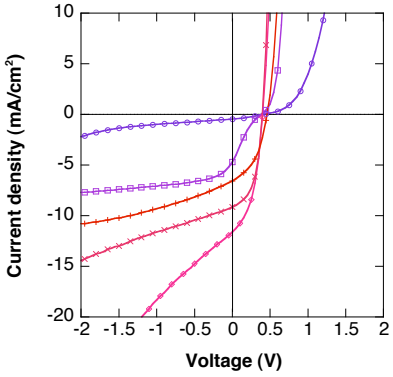

Figure 5.10: Effect of annealing on current-voltage characteristics of sintered bilayer devices. The figure shows IV curves for devices made from as-deposited films (purple circles), as well as films annealed for 5 minutes (violet squares), 15 minutes (pink diamonds), 30 minutes (orange X's), and 60 minutes (red +'s).

calcium top contact capped with aluminum, this cell demonstrates an AM1.5G power conversion efficiency of 2.9 %, with I_{sc} of 13.2 mA/cm^2, Voc of 0.454 V and FF of 0.49. Note in Figure 5.12 that all record efficiencies cited here have been validated to be self-consistent by comparing integrated EQE currents with those obtained by AM1.5G current-voltage characterization.

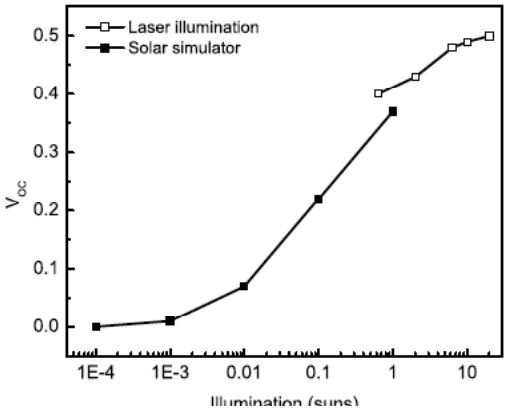

Figure 5.11: Open-circuit voltage as a function of intensity under AM1.5G solar illumination (up to 1 sun) and monochromatic illumination at peak photoresponse (from 1 sun to 20 suns).

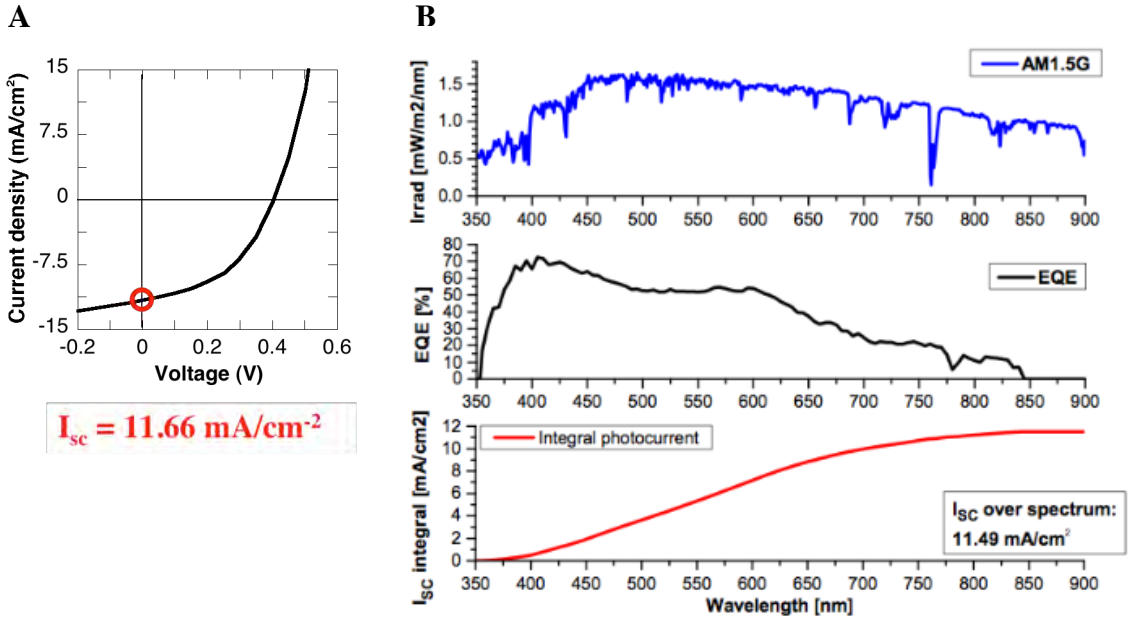

Figure 5.12: To validate the accuracy and self-consistency of characterization tools and techniques, short-circuit currents obtained under simulated AM1.5G illumination (A) were compared with those obtained by integrating EQE data with true AM1.5G solar emission spectrum (B). The results from these independent assessments were well matched, as illustrated here.

5.4.2 High resistivity transparent layer

A high resistivity transparent (HRT) buffer layer is required to mitigate the effects of shunting in sintered bilayer devices. This technique is common in certain architectures of conventional thin-film CdTe solar cells, where researchers often incorporate a thin layer of undoped tin oxide to serve as an HRT barrier (*30*). Here, we have employed atomic layer deposition for the creation of an ultra-thin HRT layer between the ITO electrode and active nanocrystal film. Atomic layer deposition allows for a high degree of control over the properties of this film through monolayer-by-monolayer variation of film thickness. Figure 5.13A illustrates the effect of an Al_2O_3 HRT layer on sintered CdTe/CdSe bilayer cells as well as the ability to optimize such a layer through atomic layer deposition.

It is clear that while a single monolayer of Al_2O_3 has negligible effect on the performance of the device; however, with a two monolayer HRT layer, the device regains it's full open-circuit voltage. With three monolayers of Al_2O_3, the HRT layer is already too thick, as the resultant devices show no further increase in V_{oc} but do exhibit a strong

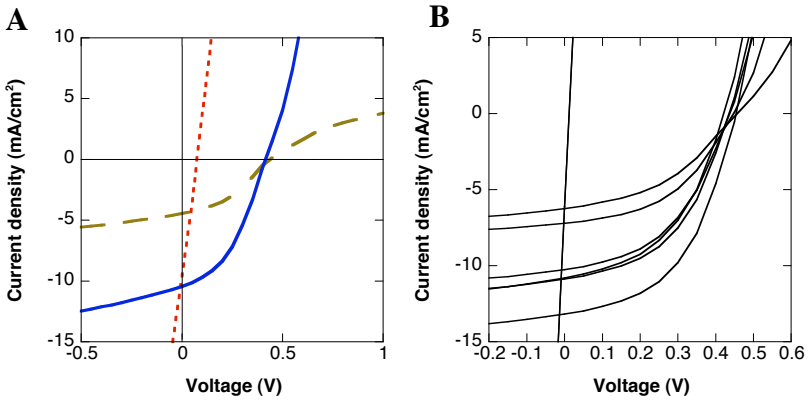

Figure 5.13: (A) illustrates control of ALD deposited HRT layers, showing effects of one (red, dotted), two (blue, solid), and three (brown, dashed) monolayers of Al_2O_3 on device performance. Homogeneity of these HRT layers may be an issue, as intra-substrate variability of performance is rather high (B).

reduction in short-circuit current. Thus it appears as though the HRT layers described here act as a tunnel barrier to shunting pathways; if the barrier is too thick, however, active current is blocked from being collected by the electrodes. Despite the high degree of control afforded in ALD deposited HRT layers, homogeneity remains an issue with this approach. In Figure 5.13B, a typical set of IV curves from eight devices fabricated on a single substrate (as described in Chapter 2) is presented, illustrating the variability of performance as a function of substrate location.

5.4.3 Environmental stability

None of the solar cells presented here, whether sintered or not, exhibited the strong sensitivity to photo-oxidation characteristic of organic-based devices; in fact, aging seems to improve rather than deteriorate their performance. Figure 5.14A shows

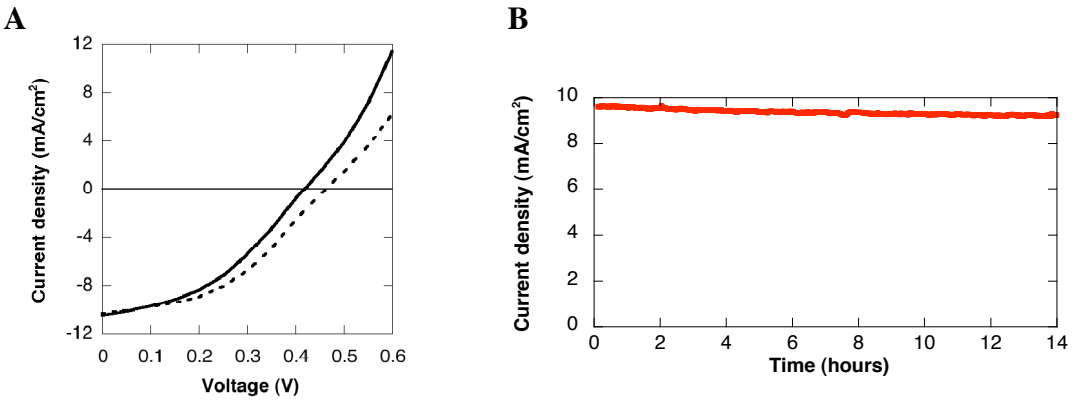

Figure 5.14: (A) Current-voltage behavior at simulated one-sun AM1.5G illumination for a typical sintered bilayer device upon first exposure to air (solid) and after 13000 hours exposure to ambient atmosphere and light. Exposure to air and ambient light results shows minimal degradation in short-circuit current, and ultimately affords a 13.6% improvement in overall power conversion efficiency. (B) Light soaking behavior of a typical sintered bilayer device. Current output dropped from 9.60 mA/cm^2 to 9.20 mA/cm^2 over 14 hours irradiation with AM1.5G light at short-circuit in air. However, illumination intensity dropped to 97% of original intensity over same period, resulting in a total degradation in short-circuit current of only 1.3%.

the AM1.5G full-sun behavior of a typical sintered device characterized in air before and after 13,000 hours' exposure to ambient atmosphere and lighting. The cell shows only a 1.4% decrease in short-circuit current, while the fill-factor rose 4.4% and the open-circuit voltage increased by over 10%. Overall, the atmospheric aging resulted in a 13.6% increase in efficiency. Light soaking at short-circuit for 14 hours under simulated AM1.5G illumination revealed less than 2% degradation in photocurrent (Figure 5.14B). These phenomena serve to illustrate the robustness of this system over its organic counterparts.

5.5 Conclusion

This demonstration introduces the first solar cells based entirely on colloidal semiconductor nanocrystals. They are ultra-thin, solution-processed, and stable in ambient environments. Comprised of dense nanocrystal films that mirror the basic properties of semiconducting polymers, these cells function as a new class of diffusion assisted donor-acceptor heterojunction. Sintering is found to enhance the performance of these devices, allowing for air-stable power conversion efficiencies up to 2.9%. The nanocrystal solar cells presented here offer a new research direction and serve as a key development toward achieving stable and low-cost solar energy conversion.

Supplemental methodology

I. Materials. Cadmium oxide (CdO) (99.99+ %), Tellurium (Te) (99.8 %, 200 mesh), Selenium (Se) (99.999%, 100 mesh), and tri-*n*-octylphosphine oxide ($C_{24}H_{51}OP$ or TOPO, 99 %) were purchased from Aldrich. *n*-Octadecylphosphonic acid ($C_{18}H_{39}O_3P$ or ODPA), *n*-Tetradecylphosphonic acid ($C_{14}H_{31}O_3P$ or TDPA) and Octylphosphonic acid ($C_8H_{19}O_3P$ or OPA), *n*-Hexylphosphonic acid ($C_6H_{15}O_3P$ or HPA), were purchased from PolyCarbon Industries, Inc. Trioctylphosphine (TOP) (97 %) was purchased from Strem Chemicals. All solvents used were anhydrous, purchased from Aldrich, and used without any further purification.

II. Synthesis of CdSe and CdTe nanorods. All manipulations were performed using standard air-free techniques. In a typical synthesis of CdSe [CdTe] rods, a mixture of 710 mg TDPA, 160 mg HPA, 3.00 g TOPO, and 200 mg CdO [812 mg ODPA, 315 mg OPA, 2.65 g TOPO, and 200 mg CdO] was degassed at 120 ºC for 60 minutes in a 25 ml three-neck flask connected to a Liebig condenser. It was heated slowly under Ar until the CdO decomposed and the solution turned clear and colorless. Next, 1.5 g of TOP were added, and the temperature was further raised to 300 ºC [320 ºC]. Next, 73 mg of selenium dissolved in 416 mg of TOP [61 mg of tellurium dissolved in 552 mg of TOP] were rapidly injected to the vigorously stirring precursors and particles were allowed to grow for 5 minutes [4 minutes] before the heat was removed to stop the reaction. After cooling the solution to 70 ºC, 3–4 ml anhydrous toluene were added to the flask, and the dispersion was transferred to an Ar drybox. The minimum amount of anhydrous isopropanol required to precipitate the nanocrystals after centrifugation was added to the

dispersion. This prevented potential co-precipitation of the Cd-phosphonate complex. After removing the supernatant, the precipitate was re-dissolved twice in toluene and re-precipitated with isopropanol.

III. Device fabrication. After synthesis, nanocrystals were dispersed in 20 mL pyridine and stirred under reflux overnight, allowing for comprehensive ligand exchange. Nanocrystals were then precipitated with hexane, washed with toluene, and redissolved in approximately one mL pyridine. These highly concentrated solutions were ultrasonicated for ca. 30 minutes and then passed through a 0.4 μm Teflon filter before spin-casting. Nanocrystal films were spin-cast at 1500-2000 rpm onto glass substrates coated with 150 nm ITO (Thin Film Devices Inc., resistivity 20 ohms/sq) and a high resistivity transparent layer of 2Å Al_2O_3 deposited by atomic layer deposition. To create bilayer structures, a single film was spin-cast and then heated for 15 minutes at 200 degrees C to remove excess solvent and allow for spin-casting of the second film. For sintering, a saturated solution of $CdCl_2$ in methanol was spin-cast onto standard bilayer samples at 1500rpm, afterwhich the samples were heated at 400 C in oxygen for 15 minutes. Finally, all samples were held at ca. 10^{-6} torr overnight, afterwhich top electrodes were deposited by thermal evaporation through a shadow mask, resulting in individual devices with 0.03 cm^2 nominal area.

III. Device characterization. Simulated AM1.5G illumination was obtained with a Spectra Physics Oriel 300W Solar Simulator with AM1.5G filter set. The integrated intensity was set to 100 mW/cm^2 using a thermopile radiant power meter (Spectra Physics Oriel, model 70260) with fused silica window, and verified with a Hamamatsu

S1787-04 diode. Intensity was controlled to be constant throughout measurements with a digital exposure controller (Spectra Physics Oriel, model 68950). Short-circuit currents obtained under simulated AM1.5G illumination were well matched with those obtained by integrating EQE data with the true AM1.5G solar emission spectrum.

References and notes

1. J. A. Barker, C. M. Ramsdale, N. C. Greenham, *Physical Review B* **67** (FEB 15, 2003).
2. B. A. Gregg, M. C. Hanna, *Journal of Applied Physics* **93**, 3605 (MAR 15, 2003).
3. J. J. M. Halls *et al.*, *Nature* **376**, 498 (AUG 10, 1995).
4. G. Yu, J. Gao, J. C. Hummelen, F. Wudl, A. J. Heeger, *Science* **270**, 1789 (DEC 15, 1995).
5. P. Peumans, V. Bulovic, S. R. Forrest, *Applied Physics Letters* **76**, 2650 (MAY 8, 2000).
6. S. E. Shaheen *et al.*, *Applied Physics Letters* **78**, 841 (FEB 5, 2001).
7. W. U. Huynh, J. J. Dittmer, A. P. Alivisatos, *Science* **295**, 2425 (MAR 29, 2002).
8. K. M. Coakley, M. D. McGehee, *Applied Physics Letters* **83**, 3380 (OCT 20, 2003).
9. S. Kim, B. Fisher, H. J. Eisler, M. Bawendi, *Journal of the American Chemical Society* **125**, 11466 (SEP 24, 2003).
10. D. J. Milliron *et al.*, *Nature* **430**, 190 (JUL 8, 2004).
11. D. S. Ginger, N. C. Greenham, *Journal of Applied Physics* **87**, 1361 (FEB 1, 2000).
12. N. Y. Morgan *et al.*, *Physical Review B* **66** (AUG 15, 2002).
13. J. Heitmann *et al.*, *Physical Review B* **69** (MAY, 2004).
14. Employing the effective mass approximation, bulk energy levels were modified to account for quantum confinement. Electron affinities for CdSe and CdTe rods were calculated to be -2.7 and - 2.3 eV respectively. Ionization energies for CdSe and CdTe rods were calculated to be -4.4 and -5.2 eV respectively.
15. Information on materials and methods is available as supporting material.
16. Results presented are based on devices utilizing the standardized syntheses of CdTe and CdSe described above - other syntheses have yielded slightly different results. For instance, devices with open circuit voltages as high as 0.6 have been achieved by varying nanocrystal diameter; a thorough description of this dependence will be described elsewhere.
17. S. M. Sze, *Physics of Semiconductor Devices* (John Wiley and Sons, New York, 1981), pp.
18. A. L. F. a. R. H. Bube, *Fundamentals of Solar Cells* (Academic Press, New York, 1983), pp.
19. M. Shim, C. J. Wang, D. J. Norris, P. Guyot-Sionnest, *Mrs Bulletin* **26**, 1005 (DEC, 2001).
20. The lower quantum efficiency of blend structures as compared with bilayers may be attributed to an increased succeptibility to non-geminate recombination.
21. N. C. Greenham, X. G. Peng, A. P. Alivisatos, *Physical Review B* **54**, 17628 (DEC 15, 1996).
22. Note: spectral oscillations in the data are attributed to coherent interactions with optical phonons in the crystals. Pump probe experiments done in collaboration with Rupert Huber, Lawrence Berkeley National Laboratory.
23. C. J. Brabec *et al.*, *Advanced Functional Materials* **11**, 374 (OCT, 2001).

24. C. J. Brabec *et al*., *Thin Solid Films* **403**, 368 (FEB 1, 2002).
25. B. Q. Sun, H. J. Snaith, A. S. Dhoot, S. Westenhoff, N. C. Greenham, *Journal of Applied Physics* **97** (JAN 1, 2005).
26. L. S. Li, J. T. Hu, W. D. Yang, A. P. Alivisatos, *Nano Letters* **1**, 349 (JUL, 2001).
27. B. E. McCandless, L. V. Moulton, R. W. Birkmire, *Progress in Photovoltaics* **5**, 249 (JUL-AUG, 1997).
28. These ultrathin cells exhibit sub-optimal absorptivity, with average optical density of approximately 0.7. This assumes full back contact reflection such that incident light passes through the film twice.
29. Short-circuit currents obtained under simulated AM1.5G illumination were well matched with those obtained by integrating EQE data with the true AM1.5G solar emission spectrum. Details on solar simulation is available as supporting material.
30. B. E. McCandless, K. D. Dobson, *Solar Energy* **77**, 839 (2004).

Chapter 6

Conclusion

Colloidal inorganic nanostructures offer great potential for reducing processing costs and improving efficiencies of solar photovoltaic technologies. Semiconductor nanocrystals can be synthesized in bulk at low temperatures and processed in solution to allow for high throughput and wide area deposition. Moreover, they inherently constitute well-suited building blocks for highly efficient photovoltaic power conversion, often boasting tunable electronic properties, strong solar absorption and high carrier mobilities. Still, despite their many benefits, nanoscale technologies generally share two major obstacles to commercialization – integration and stability. Integrating nanostructures into useful macroscopic devices often proves difficult, requiring either high processing costs or high tolerance to defects and disorder in the system. This alone can be an insurmountable barrier for many nanotechnologies; however, the development of useful nanotechnologies is also often impeded by issues related to environmental stability. Indeed, the prototypical photovoltaic technologies based on low-dimensional colloidal nanocrystals suffered drastically from both these issues.

This dissertation presents the results of a research agenda aimed at improving integration and stability in nanocrystal-based solar cells through advances in active materials and device architectures. The introduction of 3-dimensional nanocrystals illustrates the potential for improving transport and percolation in hybrid solar cells, and enables novel fabrication methods for optimizing integration in these systems. Fabricating cells by sequential deposition yields solution-based assembly of hybrid

composites with controlled and well-characterized dispersion and top-electrode contact. Hyperbranched nanocrystals emerge as a nearly ideal building block for hybrid cells, allowing the controlled morphologies targeted by templated approaches to be achieved in a simply fabricated solution-cast device. In addition to offering practical benefits to device processing, these approaches offer fundamental insight into the operation of hybrid solar cells, shedding light on key phenomena such as the roles of electrode-contact and percolation behavior in these cells. Finally, all-inorganic nanocrystal solar cells represent a wholly new cell concept, illustrating that donor-acceptor charge transfer and directed carrier diffusion can be utilized in a system with no organic components and that nanocrystals may act as building blocks for efficient, stable, and low-cost thin-film solar cells.

The research in this dissertation represents a concerted effort to improve the performance and processing of nanocrystal-based solar cells. No one approach or innovation developed here affords a complete solution, but the insights and innovations that this work contributes will hopefully accelerate our ability to understand and develop a versatile, low-cost PV solution that is efficient and stable enough to make a large-scale impact in displacing fuel-based electricity generation world-wide.